

Measuring the basic parameters of neutron stars using model atmospheres

V. F. Suleimanov^{1,2}, J. Poutanen^{3,4}, D. Klochkov¹, and K. Werner¹

¹ Institut für Astronomie und Astrophysik, Kepler Center for Astro and Particle Physics, Universität Tübingen, Sand 1, 72076 Tübingen, Germany

² Kazan Federal University, Kremlevskaja str., 18, Kazan 420008, Russia

³ Tuorla Observatory, Department of Physics and Astronomy, University of Turku, Väisäläntie 20, FI-21500 Piikkiö, Finland

⁴ Nordita, KTH Royal Institute of Technology and Stockholm University, Roslagstullsbacken 23, SE-10691 Stockholm, Sweden

Received: date / Revised version: date

Abstract. Model spectra of neutron star atmospheres are nowadays widely used to fit the observed thermal X-ray spectra of neutron stars. This fitting is the key element in the method of the neutron star radius determination. Here, we present the basic assumptions used for the neutron star atmosphere modeling as well as the main qualitative features of the stellar atmospheres leading to the deviations of the emergent model spectrum from blackbody. We describe the properties of two of our model atmosphere grids: (i) pure carbon atmospheres for relatively cool neutron stars (1–4 MK) and (ii) hot atmospheres with Compton scattering taken into account. The results obtained by applying these grids to model the X-ray spectra of the central compact object in supernova remnant HESS 1731–347, and two X-ray bursting neutron stars in low-mass X-ray binaries, 4U 1724–307 and 4U 1608–52, are presented. Possible systematic uncertainties associated with the obtained neutron star radii are discussed.

PACS. XX.XX.XX No PACS code given

1 Introduction

The fundamental problem driving the study of neutron stars (NSs) is associated with unknown physical properties of super-dense matter in the cores of these objects. It is also known as the problem of the neutron star equation of state (EOS). To determine the EOS, one would need to measure simultaneously the mass and radius of a NS. Existing theoretical models of EOS predict different mass-radius relations for NSs [1]. Various observational methods have been developed to constrain this relation using observations [2, 3].

One of the well developed methods is based on fitting the NS X-ray spectral continua with numerically computed model NS atmosphere spectra. Here, we present the basic ideas of this method and the fundamental properties of NS atmospheres important for accurate measurements of the NS masses and radii. We consider atmospheres of weakly magnetized NSs only (surface magnetic field $B < 10^8 - 10^9$ G).

Many atmosphere models have been computed almost twenty years ago, shortly after the first isolated NSs had been discovered [4]. Most of the groups [5, 6, 7] have computed NS atmospheres composed of light elements (hydrogen and helium) because heavy elements should have sunk due to gravitational separation [8, 9, 10]. A number of works is dedicated to fitting the thermal X-ray spectra

of isolated NSs and the NSs in low-mass X-ray binaries (LMXBs) in quiescence situated in globular clusters with known distances to restrict their masses and radii [11, 12, 13].

The same model NS spectra were fitted to the observed X-ray spectra of the point-like soft X-ray sources in the centers of some supernova remnants – a special group of NSs referred to as central compact objects (CCOs) [14]. The X-ray spectrum of the youngest NS of this type located in Cas A was also fitted with hydrogen model atmospheres [15]. These authors found that this model assuming a homogeneously emitting stellar surface gives a size of the emitting region of about 4 – 5.5 km, compatible with a strange quark star only. A possible solution to this problem was suggested by Ho & Heinke [16], who have found that a pure carbon NS atmosphere model gives a reasonable NS size of 10 – 14 km. Moreover, the same authors later have claimed an unusually rapid cooling of the CCO in Cas A [17, 18, 19], but this result has been questioned by Posselt et al. [20]. Recently, model spectra of pure carbon NS atmospheres were successfully applied to fit the X-ray spectrum of the CCO in HESS J1731–347 [21, 22] using our models [23]. We describe the obtained results in the current review.

X-ray bursting NSs in LMXBs are also widely used to measure the NS masses and radii [24]. Thermonuclear

burning at the bottom of the freshly accreted matter during an X-ray burst can be so intense that the luminosity L reaches the Eddington limit L_{Edd} . This can be used to obtain additional constraints on the NS mass and radius [25, 26, 27, 28, 29, 30].

Strong photon-electron interaction in hot NS atmospheres of X-ray bursting NSs leads to blackbody-like emergent spectra [31, 32, 33, 34, 35, 36, 37], such that the observed spectra of X-ray bursts can be fitted well with a blackbody [38]. In fact, the emergent spectra are not blackbody but are close to the diluted blackbody. Recently, we computed extended grids of hot NS atmospheres in a wide range of the input parameters [36, 37, 39]. Based on these computations, we also proposed a new cooling tail method for determination of the NS mass and radius using X-ray bursts with a photospheric radius expansion [36, 40]. This method is described in our review in detail as well as the results of the application of this method to the NSs in LMXBs 4U 1724–307 [40] and 4U 1608–52 [41]. For the most recent analysis of a carefully selected sample of bursts and the resulting constraints on the equation of state, we refer to ref. [42].

In principle, the atmosphere model spectra can be directly fitted to the data to obtain the constraints on the NS parameters [43, 44], but the quality of the data as well as a weak dependence of the spectra on gravity will preclude that in the nearest future.

2 Radius measurements of an ideal neutron star

2.1 Spectral fitting

Let us consider an isolated non-rotating thermally emitting homogeneous neutron star with an intrinsic luminosity L , mass M and radius R at a known distance D . In this case, the spectral flux density F_ν at Earth can be computed as

$$F_\nu = \mathcal{F}_{\nu,\infty} K = \mathcal{F}_{\nu,\infty} \frac{R_\infty^2}{D^2} = \frac{\mathcal{F}_{\nu(1+z)} R^2}{(1+z) D^2}. \quad (1)$$

Here $K = (R_\infty/D)^2$ is the normalization factor and

$$\mathcal{F}_{\nu,\infty} = \frac{\mathcal{F}_{\nu(1+z)}}{(1+z)^3} \quad (2)$$

is the undiluted observed spectral flux density, formally attributed to the apparent neutron star surface. The connection (2) between $\mathcal{F}_{\nu,\infty}$ and the intrinsic NS emergent spectral flux density \mathcal{F}_ν (the spectrum) can be derived using Liouville's theorem for photons (see, e.g. [45, 46]). The *apparent* NS radius measured by an observer at infinity $R_\infty = R(1+z)$ is larger than the intrinsic radius because of light bending, and the gravitational redshift z is related to the NS parameters as

$$1+z = (1 - 2GM/c^2 R)^{-1/2}. \quad (3)$$

The intrinsic spectrum \mathcal{F}_ν can be computed theoretically, and in general depends on the effective temperature T_{eff} , NS gravity g and chemical composition. The effective temperature is related to the intrinsic bolometric flux $\mathcal{F} = \int \mathcal{F}_\nu d\nu$ as:

$$\sigma_{\text{SB}} T_{\text{eff}}^4 = \mathcal{F} = \frac{L}{4\pi R^2}, \quad (4)$$

where L is the NS luminosity measured at the surface and σ_{SB} is Stefan-Boltzmann constant. The surface gravity accounting for the general relativity effect is

$$g = \frac{GM}{R^2} (1+z). \quad (5)$$

The bolometric observed flux can be easily obtained from eq. (1):

$$F = \int F_\nu d\nu = \frac{R_\infty^2}{D^2} \frac{\mathcal{F}}{(1+z)^4} = K \frac{\sigma_{\text{SB}} T_{\text{eff}}^4}{(1+z)^4}. \quad (6)$$

Thus if we know the observed flux as well as the redshifted, intrinsic NS spectrum $\mathcal{F}_{\nu,\infty}$ (or the redshifted effective temperature $T_{\text{eff}}/(1+z)$), and the distance D , we can find the apparent NS radius R_∞ . A curve of a constant apparent radius in the $M - R$ plane (shown by the dashed line in fig. 1) can constrain the NS radius, because the mass is limited within a relatively narrow range 1.2–2 M_\odot . It is clear, however, that the shape of the emitted spectrum is equally important for this method as the distance to the NS.

2.2 Eddington luminosity

We consider NSs that can reach the Eddington luminosity, which is determined by the balance of the surface gravity g and the radiative acceleration at the NS surface

$$g_{\text{rad}} = \frac{1}{c} \int_0^\infty \kappa_\nu \mathcal{F}_{\nu,\text{Edd}} d\nu, \quad (7)$$

where κ_ν is the opacity of the NS atmosphere. Because the opacity depends on the local physical parameters of the matter, such as temperature T , density ρ , and chemical composition, the Eddington luminosity is specific to every radiating astrophysical object. Therefore, the coherent Thomson electron scattering opacity

$$\kappa_e = \sigma_T \frac{N_e}{\rho} \approx 0.2 (1+X) \text{ cm}^2 \text{ g}^{-1} \quad (8)$$

is commonly used to determine the Eddington luminosity. Here $\sigma_T = 6.65 \times 10^{-25} \text{ cm}^2$ is the Thomson cross-section, N_e is the electron number density, and X is the hydrogen mass fraction. The Thomson opacity does not depend on the local matter properties because $N_e \sim \rho$, but depends on X . It allows us to define the intrinsic bolometric Eddington flux

$$\mathcal{F}_{\text{Edd}} = \int_0^\infty \mathcal{F}_{\nu,\text{Edd}} d\nu = \frac{gc}{\kappa_e}, \quad (9)$$

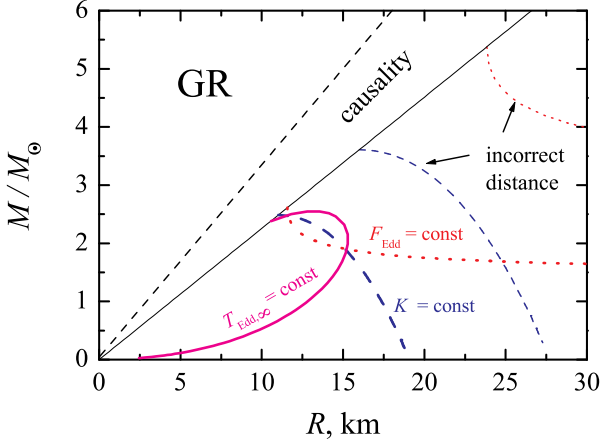


Fig. 1. The constraints on M and R of the neutron star from various observables. The solid curve gives the relation obtained for the Eddington temperature $T_{\text{Edd},\infty} = 1.64 \times 10^7$ K using eq. (13) for a pure hydrogen atmosphere ($X = 1$). The dotted curves are for the Eddington flux $F_{\text{Edd}} = 5.61 \times 10^{-8} \text{ erg s}^{-1} \text{ cm}^{-2}$ (using eq. (12)), dashed curves are for $K = 1.37 \times 10^{-32}$ (from eq. (1)), shown for two different distances, $D = 5.3$ kpc (thick curves) and 7.7 kpc (thin curves). For a larger distance there are no solutions (the curves shown by thin lines do not intersect).

and the intrinsic Eddington luminosity

$$L_{\text{Edd}} = 4\pi R^2 \mathcal{F}_{\text{Edd}} = \frac{4\pi G M c}{\kappa_e} (1+z). \quad (10)$$

The observed Eddington luminosity is lower:

$$L_{\text{Edd},\infty} = \frac{L_{\text{Edd}}}{(1+z)^2} = \frac{4\pi G M c}{\kappa_e} (1+z)^{-1}, \quad (11)$$

here one factor $1+z$ accounts for the photon energy redshift, while another for the time dilation. The observed bolometric Eddington flux at Earth can also be defined as

$$F_{\text{Edd}} = \frac{L_{\text{Edd},\infty}}{4\pi D^2}. \quad (12)$$

Therefore, if we know that the NS luminosity is equal to the Eddington luminosity at a certain time and measure the bolometric flux at this time, we obtain additional constraints on the NS mass and radius. Apart from the distance, the hydrogen mass fraction X is another crucial uncertainty here. The corresponding curve $L_{\text{Edd},\infty} = \text{const}$ in the $M - R$ plane is also shown by the dotted curve in fig. 1. Because both R_∞ and $L_{\text{Edd},\infty}$ depend on the distance D , the corresponding curves $R_\infty = \text{const}$ and $L_{\text{Edd},\infty} = \text{const}$ are also distance dependent. The correct values of M and R of the NS are located at the crossing points of the two curves.

It is easy to combine two observed values, F_{Edd} and K , which both depend on distance D , to one value, which

is independent of D

$$\frac{F_{\text{Edd}}}{K} = \frac{gc}{\kappa_e} (1+z)^{-4} = \frac{\mathcal{F}_{\text{Edd}}}{(1+z)^4} = \sigma_{\text{SB}} \left(\frac{T_{\text{Edd}}}{1+z} \right)^4. \quad (13)$$

The new quantity F_{Edd}/K is simply the redshifted intrinsic Eddington flux $\mathcal{F}_{\text{Edd},\infty} = \mathcal{F}_{\text{Edd}}(1+z)^{-4}$. Here, we also introduced the Eddington effective temperature T_{Edd} , which is a suitable parameter describing the Eddington flux.

The contour $T_{\text{Edd},\infty} = T_{\text{Edd}}/(1+z) = \text{const}$ in the $M - R$ plane shown in fig. 1 by the solid curve corresponds to all possible crossing points of the curves $K = \text{const}$ and $F_{\text{Edd}} = \text{const}$ at all possible values of D . This curve allows to evaluate the NS radius even without any information about the distance. We note, however, that the result does depend on the assumed hydrogen mass fraction which affects the Thomson opacity and thus the Eddington limit.

3 Neutron star model atmospheres

3.1 Basic properties

The atmosphere of a neutron star is a relatively thin outer plasma envelope, where the escaping radiation is formed. To obtain a correct model emergent spectrum, a complete physical model of the atmosphere needs to be computed. Therefore, all the hydrodynamical conservation laws such as mass, energy, and momentum conservation (the Euler equations) have to be taken into account together with an appropriate equation of state of the matter.

3.1.1 Steady state approximation

Usually standard steady state atmospheres without any large-scale movements are considered, and the Euler equations are reduced to the hydrostatical equilibrium equation. The envelope lies above a source of energy, a hot crust of an isolated cooling NS or a thermonuclear burning layer in X-ray bursting NS, and does not have any own local energy sources. Therefore, the thermal energy is just transported through the atmosphere under a local energy balance. Energy is transported by radiation and a correct radiative transfer description is the most important part of atmosphere modelling. A possible energy transport by convection or by electron conductivity is ignored. Convection is possible in the NS envelopes at early stages of X-ray bursts. The electron conductivity could be significant at the deepest atmosphere layers only, where the electron degeneracy becomes significant. Fortunately, it only happens in the atmosphere layers, which are much deeper than those where escaped photons originate even for low-temperature atmospheres [23], not affecting the emergent spectra. Another important approximation is the absence of any external flux of radiation or fast particles bombarding the outer atmospheric boundary.

A detail description of the NS atmospheres modelling is given in the Sect. 3.2. Here, we describe the structure of NS atmospheres which determine the emergent model spectra.

3.1.2 Plane-parallel approximation and hydrostatic equilibrium

The thickness of NS atmospheres is negligible compared to the NS radius. A typical pressure-scale height is about

$$h_p \approx \frac{kT}{\mu m_H (g - g_{\text{rad}})} = 1.3 T_6 (g - g_{\text{rad}})_{14}^{-1} \text{ cm}, \quad (14)$$

where $\mu = 0.62$ is the mean molecular weight of a particle in a fully ionized solar mix plasma, and $m_H = 1.67 \times 10^{-24} \text{ g}$ is the proton mass (here and later, we use the notation for some variables in cgs units $Q_x = Q \times 10^{-x}$). Therefore, almost all NS atmospheres can be treated in the plane-parallel approximation where all the physical variables, such as density ρ and temperature T , depend on the vertical geometrical coordinate s only. Using the column density m

$$dm = -\rho ds, \quad (15)$$

instead of s is even more suitable in this case. We note, that $m = 0$ corresponds to the upper atmospheric boundary.

Under the described assumptions, the hydrostatic equilibrium equation

$$\frac{dP}{dm} = g - g_{\text{rad}} \quad (16)$$

has the integral

$$P = \rho \frac{kT}{\mu m_H} \approx m (g - g_{\text{rad}}). \quad (17)$$

Here, P is the gas pressure and the equation of state for an ideal gas is assumed. We discuss below the applicability of this approximation.

3.1.3 Chemical composition

The chemical composition of the NS atmosphere is the most uncertain model parameter. Atmospheres of non-accreting NSs have to be chemically pure and consist of the lightest chemical element of the envelope only because of gravitational separation [8, 9, 10]. The reason for this is a short characteristic sedimentation time (a diffusion time through a pressure-scale height h_p) of any heavy element with $A/Z \approx 0.5$ relative to hydrogen for NS atmosphere

$$t_{\text{sed}} \approx 0.04 \frac{\rho^{1.3}}{g_{14}^2 T_6^{0.3}} \text{ sec} \quad (18)$$

(see [47] and references there).

Atmospheres of accreting NSs have the same mixture of elements as the donor star if the accretion rate is much faster than the process of gravitational separation. A typical atmosphere thickness is about $m_{\text{atm}} \approx 100 \text{ g cm}^{-2}$, and this surface density would be displaced by accreted matter for $t_{\text{sed}} \approx 0.04 \text{ sec}$ at a mass accretion rate

$$\begin{aligned} \dot{M}_{\text{cr}} &= 4\pi R^2 \frac{m_{\text{atm}}}{t_{\text{sed}}} \approx 3 \times 10^{16} R_6^2 \text{ g/s} \\ &\approx 5 \times 10^{-10} R_6^2 M_{\odot}/\text{yr}. \end{aligned} \quad (19)$$

This mass accretion rate provides a luminosity $L_{\text{cr}} \approx 6 \times 10^{36} \text{ erg/s}$, or $\approx 0.03 L_{\text{Edd}}$ for a NS with $R = 10 \text{ km}$ and $M = 1.5 M_{\odot}$. This luminosity corresponds to an effective temperature of $T_{\text{eff}} \approx 10^7 \text{ K}$, which is much higher than the blackbody temperatures of the thermally emitted NS in low-mass X-ray binaries in quiescence [48]. Therefore, the mass accretion rate in quiescence in such systems, if accretion takes place, is much lower than \dot{M}_{cr} and it disturbs the pure hydrogen composition only slightly. On the other hand, in X-ray bursters the luminosity is higher and therefore the atmosphere composition is expected to be similar to that of the accreting matter.

The lightest element can be hydrogen for NS accreting matter from the normal donor star or helium in ultra-compact binary systems with a helium white dwarf as a donor star [49], or even C and O from stripped C/O white dwarfs [50].

3.1.4 Opacity

The properties of a model atmosphere as well as features of an emergent model spectrum are determined by the interaction between photons and atmosphere particles. This interaction is described by the plasma opacity χ_{ν} and the optical depth τ_{ν} in the stellar model atmosphere theory [51]

$$d\tau_{\nu} = \chi_{\nu} dm. \quad (20)$$

The total opacity χ_{ν} is divided in two physically different parts, the electron scattering κ_e and a “true” absorption opacity κ_{ν}

$$\chi_{\nu} = \kappa_e + \kappa_{\nu}. \quad (21)$$

The absorption opacity κ_{ν} describes processes with photon destruction, such as photoionization (bound-free processes), transitions between electron energy levels in atoms and ions (bound-bound processes), and interactions between free electrons and charged nuclei (free-free processes):

$$\kappa_{\nu} \sim \sigma_{\nu} \frac{N_e N^+}{\rho}. \quad (22)$$

Here, σ_{ν} is the cross-section of a specific process and N^+ is the number density of the ions involved.

The photon energy transforms to the thermal motion of plasma particles in these processes. In the opposite “true” emission processes a new-born photon takes part of the thermal energy of the particles and carries the information about the temperature in the birth-place into other parts of the atmosphere. The absorption opacity is almost linearly proportional to the local plasma density because two charged particles participate in these processes.

A photon does not disappear in a scattering off an electron. It simply changes its propagation direction. The momentum and energy exchange between the photon and electron are significant only for temperatures in excess of 10^7 K and photon energies $E = h\nu$ above 10 keV . Therefore, the electron scattering in relatively cool NS atmospheres with $T_{\text{eff}} \sim 10^6 \text{ K}$ can be considered as a coherent

process and κ_e does not depend on the local properties in a fully ionized plasma. However, the energy exchange in electron scatterings is much more significant in luminous NS atmospheres with $T_{\text{eff}} \geq 10^7$ K, and determines the emergent spectrum. This case of Compton scattering will be considered separately.

3.1.5 Plasma equation of state

The equation of state of the ideal gas as well as the local thermodynamical equilibrium (LTE) provide relatively good approximations for NS atmospheres [52]. The LTE assumption allows us to compute number densities of different ionization states for all chemical species together with number densities of all excited (and ground) states of every ionization state, using Saha and Boltzmann equations. Formally, this assumption means that any transitions between different levels of a given ionization state of a certain chemical element together with the ionization and recombination processes are determined by interactions with free electrons only. This assumes that the radiative transitions like photoionization and photo-recombination are negligible compared to collisions with electrons. In fact, the radiative transitions cannot be ignored, but the deviations from LTE are not significant because of the thermal-like radiation field in the NS atmospheres. Therefore, LTE is a sufficiently good approximation for low-temperature NS atmospheres because of their high densities and thermal radiation field. Almost all of the most abundant chemical elements are fully ionized in high-temperature NS atmospheres making the LTE assumption reasonable. We can expect significant deviations from LTE in atmospheres of luminous NSs with enhancement abundances of iron group chemical elements. The pressure ionization and level dissolution effects are important for population computations, but they can be easily taken into account using the occupation probability formalism [53, 54], see also [55].

3.1.6 Radiation field

The radiation field in a given direction in model atmospheres is described by the specific intensity $I_\nu \sim \nu^3 N_\nu$, which is connected with the photon occupation number N_ν . The angular averaged specific intensity is referred to as mean intensity J_ν , and the first momentum of I_ν with respect to the angle H_ν describes the net rate of radiant energy flow in the atmosphere

$$J_\nu = \frac{1}{2} \int_{-1}^{+1} I_\nu d\mu, \quad H_\nu = \frac{1}{2} \int_{-1}^{+1} \mu I_\nu d\mu, \quad (23)$$

where $\mu = \cos \theta$, and θ is the angle between photon propagation direction and the normal to the plane-parallel atmosphere. We note that the Eddington flux H_ν is connected to the physical flux \mathcal{F}_ν as $4\pi H_\nu = \mathcal{F}_\nu$.

The radiation transfer equation describes the interaction between photons and plasma:

$$\mu \frac{dI_\nu}{dm} = (\kappa_\nu + \kappa_e) I_\nu - (\kappa_\nu B_\nu + \kappa_e J_\nu), \quad (24)$$

where B_ν is the Planck function. The first term on the right-hand side of the equation describes the absorption rate of photons, the second one – the emission rate of photons in a given direction due to “true” emission processes and coherent electron scattering.

3.1.7 Thermal structure

A stellar atmosphere can be divided in optically thin ($\tau_\nu < 1$) surface layers and optically thick deep layers ($\tau_\nu \gg 1$). In the optically thick layers, the thermodynamical equilibrium between radiation and plasma holds, such that $J_\nu \approx B_\nu$. The temperature of these layers is determined by diffusion of radiation, which is the first moment of the radiation transfer equation integrated over frequency

$$\frac{dB}{dm} = \frac{3}{4\pi} \kappa_R \mathcal{F}, \quad \text{or} \quad \frac{4}{3\kappa_R} \frac{dT^4}{dm} = T_{\text{eff}}^4. \quad (25)$$

Here κ_R is the Rosseland mean opacity of the plasma, which does not depend on the radiation field and can be computed in advance. In the first approximation, the Rosseland opacity can be expressed as a sum of the electron scattering opacity and Kramers opacity:

$$\kappa_R \approx \kappa_e + 5 \times 10^{24} \rho T^{-3.5} \text{ cm}^2 \text{ g}^{-1}. \quad (26)$$

This approximation is valid for a relatively hot ($T > 10^4$ K) solar mix plasma [56]. The numerical coefficient in the Kramers law is significantly smaller for a fully ionized pure hydrogen plasma, namely $\approx 6.6 \times 10^{22}$.

An approximate solution for the model atmosphere temperature structure is given by

$$T(\tau_R) \approx T_{\text{eff}} (\tau_R + q)^{1/4}. \quad (27)$$

Therefore, for the optically thick atmospheric layers, the deeper the hotter. The constant q is determined by the physical conditions in the optically thin atmospheric layers. If the atmosphere absorption opacity κ_ν depends on photon energies only slightly, the emergent spectrum will be close to the Planck function at the effective temperature, will form at $\tau_R \approx 1$ and $q \approx 0.5$. For example, this situation is realized in the Sun, where the atmosphere opacity is determined by the negative hydrogen ion H^- , and depends on the photon energy in the visual part of the spectrum only slightly.

3.1.8 Emergent spectra

There are two facts which qualitatively determine the emergent spectrum. The emergent flux prefers escaping at the less opaque parts of the possible photon energy range.

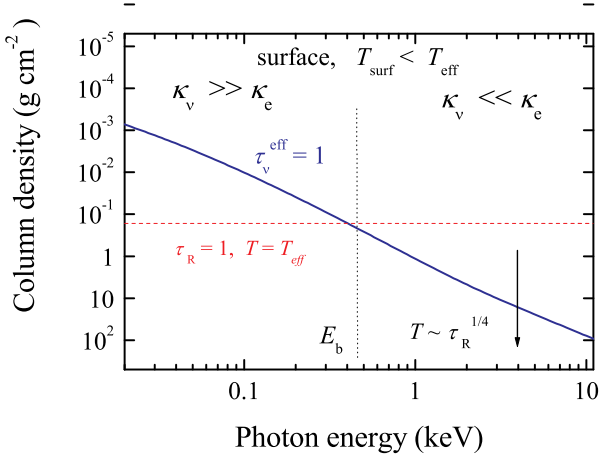


Fig. 2. The depth of the spectrum formation ($\tau_\nu^{\text{eff}} = 1$) vs. photon energy for a pure hydrogen atmosphere with $\log g = 13.9$ and $T_{\text{eff}} = 1$ MK. The division to the low and high energy bands is also shown (see text).

Numerically, it approximately coincides with the Planck function at the averaged photon birth depth m'_ν , $\mathcal{F}_\nu \approx \pi B_\nu(T(m'_\nu))$. In typical NS atmospheres, the absorption opacity as well as the photon birth depth strongly depend on photon energy. Therefore, the birth depth could deviate significantly from the depth corresponding to $\tau_R \approx 1$.

Let us consider a relatively cool pure hydrogen NS atmosphere and qualitatively describe its emergent spectrum. Hydrogen in such an atmosphere is fully ionized as $E_{\text{ion}} \approx 0.014 \text{ keV} \ll kT_{\text{eff}} \approx 0.1 \text{ keV}$, and the absorption opacity is just the bremsstrahlung opacity $\kappa_\nu \sim \rho \nu^{-3} \sim \rho E^{-3}$. It means that at every atmospheric depth m there is a limiting photon energy E_b , such that $\kappa_\nu > \kappa_e$ at $E < E_b$ and $\kappa_\nu < \kappa_e$ in the opposite case (see fig. 2). The boundary energy is shifted to larger energies with increasing m because of the increasing density.

This allows us to divide the energy band in the atmosphere at $\tau_R \approx 1$ in such two parts. The escaping flux in the low energy part approximately equals the Planck function at $\tau_\nu^a \sim \kappa_\nu m \approx 1$, $\mathcal{F}_\nu \approx \pi B_\nu(T_{\text{surf}})$. This optical depth corresponds to the surface atmosphere layers because of $\kappa_\nu > \kappa_R$ at this energy band. The emergent flux corresponds in this case to the Planck function computed for the surface temperature.

In the high energy part, photons scatter a few times after being created in a “true” emission processes before escaping because $\kappa_\nu < \kappa_e$. Therefore, the emergent flux here corresponds to the Planck function computed for the temperature at the photon birth depth. Electrons scatter photons in random directions, and we cannot just take the birth-depth at $\kappa_\nu m \approx 1$. The birth-depth for escaping photons is not so deep and can be found using the so called effective or thermalization optical depth $\tau_\nu^{\text{eff}} \sim \sqrt{\kappa_\nu(\kappa_\nu + \kappa_e)} m \approx 1$ [45]. In the considered energy band, the thermalization depths are larger than the depth $\tau_R \approx 1$. Therefore, the emergent fluxes are higher than the

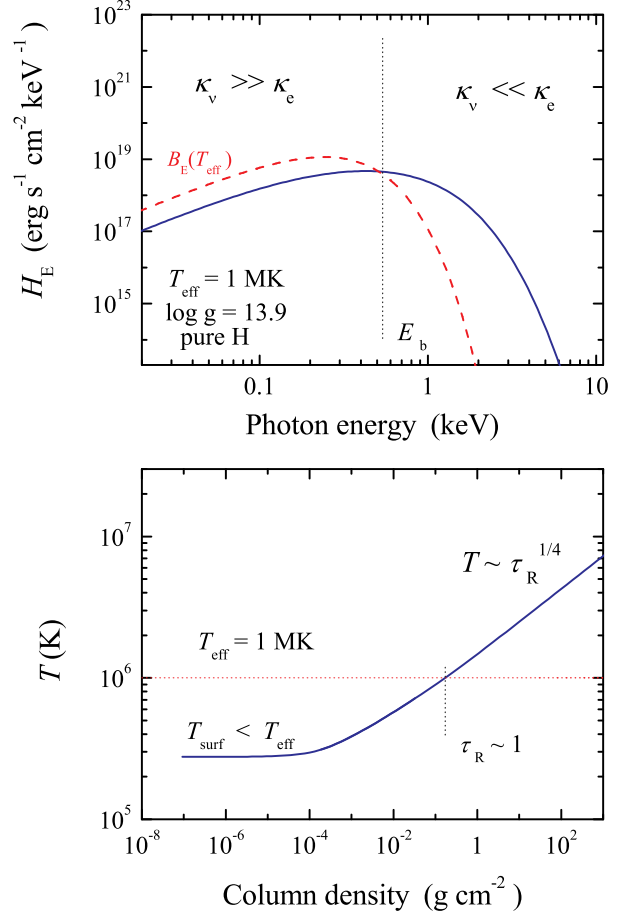


Fig. 3. The emergent spectrum (*top*) and temperature structure (*bottom*) of a pure hydrogen atmosphere with $\log g = 13.9$ and $T_{\text{eff}} = 1$ MK. The corresponding blackbody spectrum (dashed curve) is also shown in the top panel.

blackbody flux computed for the effective temperature, $\mathcal{F}_\nu \approx w_\nu \pi B_\nu(T > T_{\text{eff}})$, where $w_\nu \approx \sqrt{\kappa_\nu/(\kappa_\nu + \kappa_e)}$ is the dilution factor. We note that the thermalization depth increases with increasing photon energy such that the final emergent spectrum is much harder than $\pi B_\nu(T_{\text{eff}})$ in the high-energy part.

Since the bolometric emergent flux is conserved, the emergent flux in the low energy part has to be lower than $\pi B_\nu(T_{\text{eff}})$. This means that the surface temperature should be significantly smaller than the effective temperature, up to $T_{\text{surf}} \approx 0.2 T_{\text{eff}}$. Indeed, the surface temperature is determined by the balance between heating due to absorption of photons and cooling due to emission of photons

$$\int_0^\infty \kappa_\nu J_\nu d\nu = \int_0^\infty \kappa_\nu B_\nu(T_{\text{surf}}) d\nu. \quad (28)$$

The radiation field J_ν in the high energy band does not change at the surface, and we know that it is hard. But these hard photons are absorbed only slightly by the plasma

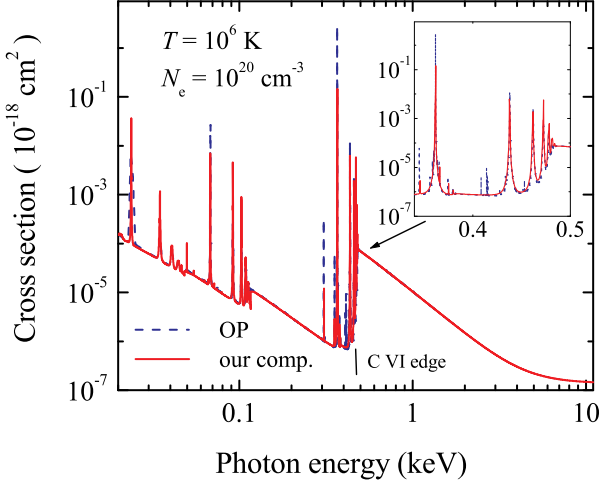


Fig. 4. Comparison of the carbon opacities published by *Opacity Project* [57] (dashed curves) and those computed by us (solid curves). The inset graph shows a zoom into the region of the Lyman-like lines. The ionization threshold energy of the C VI ion, 489 eV, is indicated by the solid vertical line. From ref. [23]

($\kappa_\nu \sim \nu^{-3}$). This absorbed energy can be easily compensated by much more effective emission at low photon energies (κ_ν is large) even at a relatively low plasma temperature.

Examples of the numerically computed temperature structures and emergent spectra of hydrogen NS model atmospheres are shown in fig. 3 to illustrate the temperature structures and emergent spectra properties described above. The helium model spectra are slightly different. However, all the features discussed above are correct for helium as well, because helium is also fully ionized in such atmospheres. The model spectra of light element NS atmospheres were computed by different authors (for review see ref. [7]).

3.1.9 Partially ionized atmospheres

Some NS envelopes might not have light elements, H or He. Let us consider a pure carbon atmosphere as an example. Carbon is not fully ionized in the considered cool NS atmospheres, because the carbon ionization potential $E_{\text{ion}}^{\text{C}} \approx 0.5 \text{ keV}$ is comparable to or higher than kT_{eff} . Therefore, the absorption opacity is much larger than in a fully ionized light element atmosphere because photoionization cross-sections are larger than the bremsstrahlung cross-section. Spectral lines also contribute significantly to the total opacity (see fig. 4).

The photoionization opacity is maximal at the photoionization edge and decreases to higher photon energy. Therefore, in the total photon energy band there is a relatively broad opaque band at $h\nu \geq E_{\text{ion}}^{\text{C}}$. The emergent flux of a carbon atmosphere in this opaque band forms in

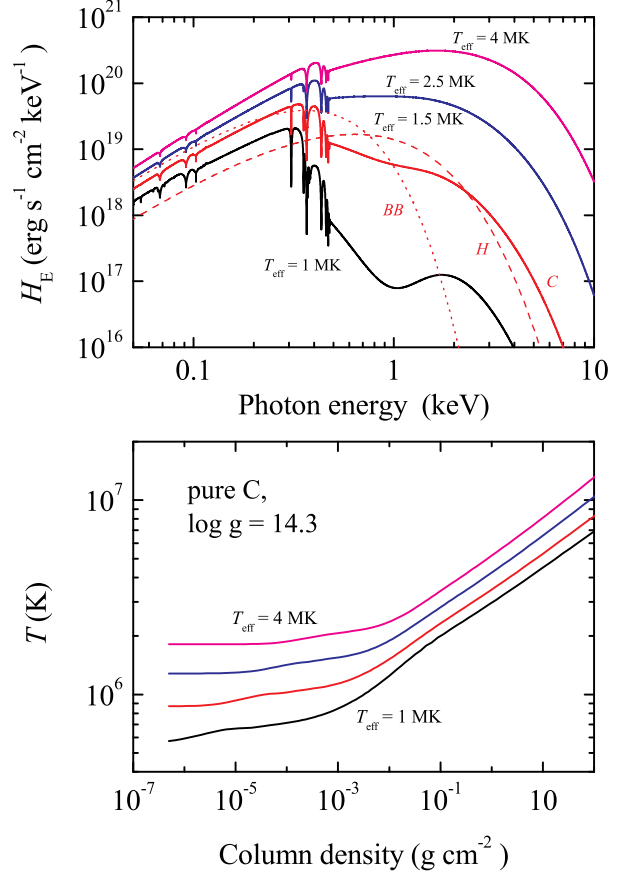


Fig. 5. Emergent spectra (top panel) and temperature structures (bottom panel) of pure carbon atmospheres with fixed $\log g = 14.3$ and a set of effective temperatures. For $T_{\text{eff}} = 1.5 \text{ MK}$, the corresponding blackbody spectrum (dotted curve) and the pure hydrogen model spectrum (dashed curve) are also shown. From ref. [20]

cool surface layers and carries a relatively small fraction of the bolometric flux. As a result, photons from a carbon atmosphere escape in the more transparent higher energy spectral band such that the high energy part of the spectrum is even harder than the corresponding part of the hydrogen/helium atmosphere spectrum. Such an “opaque band” effect is especially significant when the maximum of the effective Planck function $B_\nu(T_{\text{eff}})$ coincides with the photoionization edge, $E_{\text{ion}}^{\text{C}} \sim 3kT_{\text{eff}}$.

Examples of the temperature structures and the emergent spectra of carbon atmospheres are shown in fig. 5. By now two groups have computed extended grids of model spectra of NS carbon atmospheres [16, 23].

3.1.10 Importance of Compton scattering in hot atmospheres

The approximation of coherent electron scattering breaks down for hot luminous NS atmospheres with $kT_{\text{eff}} \geq 1 \text{ keV}$

($T_{\text{eff}} \geq 10^7$ K). Hence, Compton electron scattering instead of Thomson electron scattering has to be considered.

Let us again consider a hydrogen NS model atmosphere with $kT_{\text{eff}} \approx 2$ keV. The previously used division of the spectral energy band in two qualitatively different parts at the $\tau_R \approx 1$ depth – the low energy band with “true” absorption dominating over electron scattering and the high energy band with electron scattering as main opacity source – is still valid.

Photons created at $\tau_{\nu}^{\text{eff}} \approx 1$ are still scattered a few times before escaping. But now they exchange energy and momentum with cooler electrons in the surface atmospheric layers much more effectively. Therefore, Compton scattering supports thermodynamical equilibrium between photons and electrons up to their escape. As a result, the hard part of the emergent spectrum approaches a diluted blackbody spectrum

$$\mathcal{F}_{\nu} \approx w \pi B_{\nu}(T_c) \quad (29)$$

with the colour temperature $T_c > T_{\text{eff}}$, because the averaged escaping depth has a temperature higher than the effective temperature, and the number of photons is not enough to form a normal Planck spectrum $B_{\nu}(T_c)$. Here $w \approx f_c^{-4}$ is the dilution factor, and the colour correction factor $f_c = T_c/T_{\text{eff}} > 1$.

Compton scattering also affects the energy balance in the surface layers. The approximate energy balance equation in the diffusion (Kompaneets) approximation is

$$\int_0^{\infty} \left(\kappa_{\nu} (J_{\nu} - B_{\nu}) - \kappa_e \frac{4kT - h\nu}{m_e c^2} J_{\nu} \right) d\nu \approx 0. \quad (30)$$

The hard photons additionally heat the surface layer up to T_c at the surface where the absorption opacity is negligible because the density is low. Hence, the emergent spectrum in the low energy band could be as high as $\pi B_{\nu}(T_{\text{eff}})$ or even higher (see fig. 6). We note that Compton scattering does not change the atmospheric temperature structure in the deep optically thick layers, because Compton heating and cooling balance each other at $J_{\nu} \approx B_{\nu}$. Examples of the temperature structure and the emergent spectra of hydrogen atmosphere models with Compton scattering taken into account for a set of relative luminosities $l = \mathcal{F}/\mathcal{F}_{\text{Edd}}$ are shown in fig. 7.

The colour correction factor f_c is about 1.4–1.5 for moderately luminous NS atmospheres with $l \sim 0.5$ and slightly depends on the chemical composition of the atmosphere (see fig. 8). But f_c increases significantly, up to 1.7–1.9, for luminous atmospheres which are close to the Eddington limit. The reason for that is a strong decrease of the plasma density at $g_{\text{rad}} \approx g$, see eq. (16). It leads to a decrease of the absorption opacity and the thermalization depth is reached at relatively larger and hotter column densities.

We have computed extended grids of model spectra of hot NS atmosphere for several chemical composition and three values of $\log g$: 14.0, 14.3, and 14.6 using two approaches: a diffusion approximation for Compton scattering based on the Kompaneets equation [36] and using

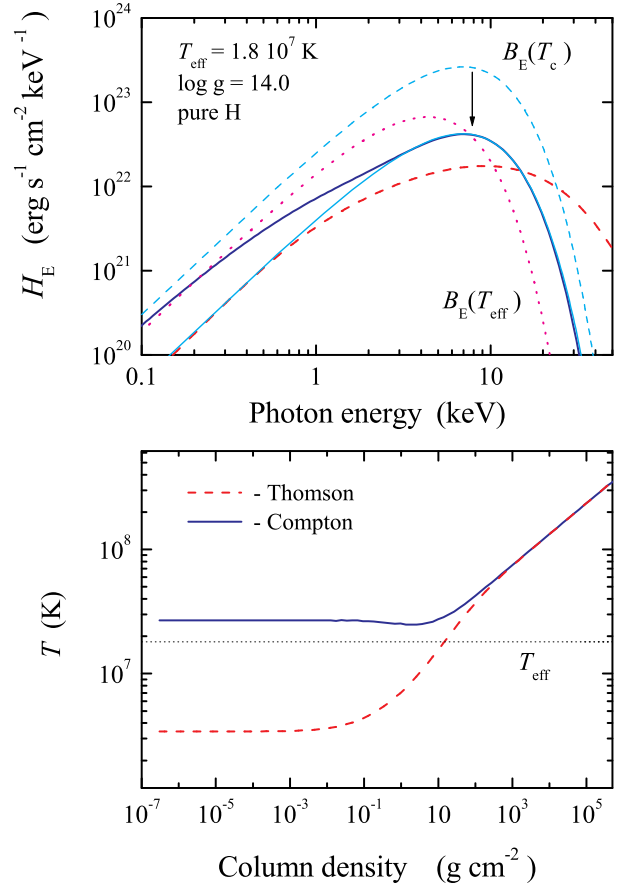


Fig. 6. The emergent spectra (top panel) and the temperature structures (bottom panel) of pure hydrogen atmospheres with $\log g = 14.0$ and $T_{\text{eff}} = 18$ MK computed taking Compton scattering (black thick solid curves) into account, and using Thomson scattering (red dashed curves). The corresponding blackbody spectrum (pink dotted curve), the diluted blackbody spectrum ($f_c = 1.58$, blue thin solid curve), and the blackbody spectrum for the colour temperature (blue thin dashed curve) are also shown in the top panel.

fully relativistic redistribution function to describe Compton scattering [37].

The model atmospheres in the latter work were computed for luminosities formally exceeding the Eddington limit ($l > 1$) defined for Thomson opacity. The reason is a well-known reduction of the electron scattering opacity at high temperatures (the Klein-Nishina effect). In fig. 9 we show the dependence of the ratio of the radiation force to the surface gravity g_{rad}/g on the depth of the atmospheric layers, which demonstrates clearly this reduction (at small column densities g_{rad}/g is always smaller than 1). We note that the ratios are smaller than unity for all relative luminosities, including $l > 1$.

The radiative acceleration can formally be represented as a product of the flux- and temperature-dependent ef-

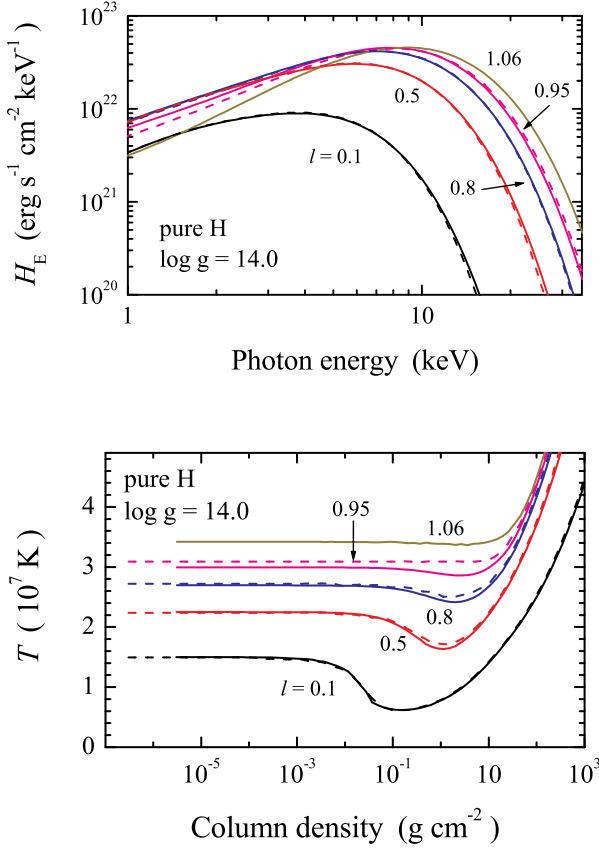


Fig. 7. The emergent spectra (top panel) and temperature structures (bottom panel) of pure hydrogen atmospheres with a fixed $\log g = 14.0$, and a set of relative luminosities. The models computed using the fully relativistic angular dependent redistribution function (solid curves) are shown together with the models computed using Kompaneets equation (dashed curves). From ref. [37].

fective opacity

$$g_{\text{rad}} = \kappa(T) \frac{\sigma_{\text{SB}} T_{\text{eff}}^4}{c}. \quad (31)$$

This expression can alternatively be written as

$$\frac{g_{\text{rad}}}{g} = l \frac{\kappa(T)}{\kappa_e}. \quad (32)$$

In the diffusion approximation, $\kappa(T)$ is given by the Rosseland mean opacity, which is well fitted by the improved Paczynski's formula [58,37]

$$\kappa_{\text{R}}(T) \approx \kappa_e \left[1 + \left(\frac{kT}{39.4 \text{ keV}} \right)^{0.976} \right]^{-1}. \quad (33)$$

The computed colour correction factors for luminous NS atmospheres are well described by the formula

$$f_c \approx \left([0.102 + 0.008X] \ln \frac{3 + 5X}{1 - g_{\text{rad}}/g} + 0.63 - 0.06X \right)^{-4/5}$$

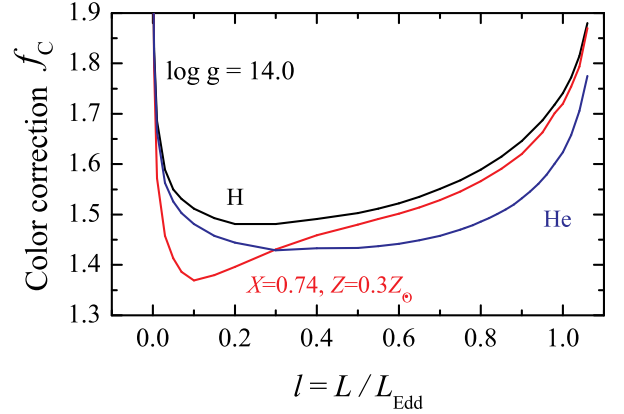


Fig. 8. The colour correction factors f_c for the model atmospheres of three chemical compositions (pure hydrogen, pure helium, and solar hydrogen/helium mix with 30% of solar heavy-element abundance) as a function of the relative luminosity l .

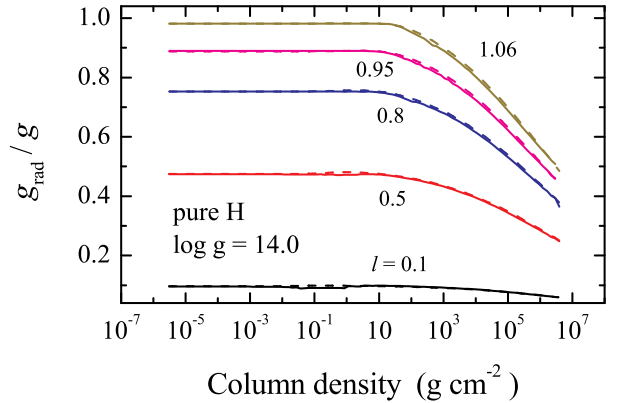


Fig. 9. Comparison of the relative radiative acceleration in pure hydrogen atmospheres computed exactly (solid curves) with the approximation given by eqs. (32) and (33) and shown by the dashed curves (nearly coinciding with the solid curves). From ref. [37].

$$\times \left(\frac{3 + 5X}{1 - g_{\text{rad}}/g} \right)^{2/15} (g_{\text{rad}}/g)^{3/20}, \quad (34)$$

which is similar to the formula suggested by Pavlov et al. [34] with numerical constants which also depend on the chemical composition. This approximation works well for $g_{\text{rad}}/g > 0.8$ (see fig. 10).

3.2 Numerical details

Under the assumptions described in Sect. 3.1 and with the given input parameters – the effective temperature T_{eff} , the surface gravity $\log g$, and the chemical composition – a

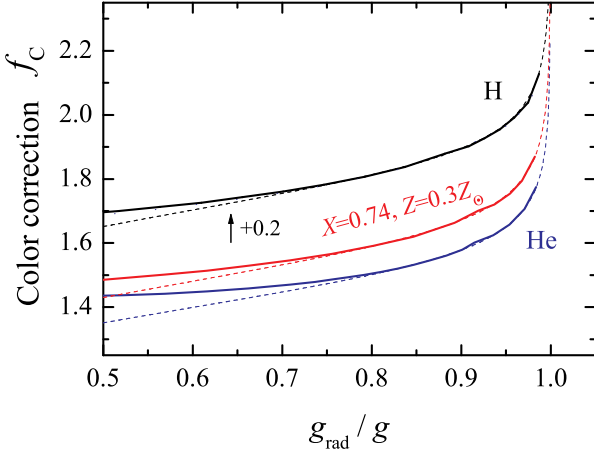


Fig. 10. The colour correction factor f_c versus g_{rad}/g for the models of various chemical compositions. Solid curves are the results of calculations (for $\log g = 14.0$), the dotted curves give the approximation (34). For clarity, the curves for pure H models are shifted upwards by 0.2. From ref. [37].

model atmosphere has to be computed numerically. Here, we describe some technical details for these computations. A more detailed description can be found in the papers dealing with specific model atmospheres [59, 60, 36, 37, 23].

3.2.1 Main equations

The structure of the NS atmosphere is described by a set of differential equations. The first one is the hydrostatic equilibrium equation (16). The second one is the radiation transfer equation for the specific intensity $I(x, \mu)$

$$\mu \frac{dI(x, \mu)}{d\tau(x, \mu)} = I(x, \mu) - S(x, \mu), \quad (35)$$

where

$$d\tau(x, \mu) = [\sigma(x, \mu) + k(x)] dm, \quad (36)$$

$x = h\nu/m_e c^2$ is the photon energy in units of electron rest mass, and $k(x)$ is the “true” absorption opacity. The source function is a sum of the thermal part and the scattering part

$$S(x, \mu) = \frac{k(x)B_x + \kappa_e S_{\text{sc}}(x, \mu)}{\sigma(x, \mu) + k(x)}, \quad (37)$$

where

$$B_x = B_\nu \frac{d\nu}{dx}, \quad (38)$$

with B_ν being the Planck function. We note that all the intensities and source functions dependent on frequency are transferred using the same relation. The scattering part of the source function $S_{\text{sc}}(x, \mu)$ as well as the electron scattering opacity $\sigma(x, \mu)$ can be considered under three different assumptions.

In the simplest case of the coherent electron scattering, acceptable at relatively low temperatures $T_{\text{eff}} < 10^6$ K, the electron scattering opacity is given by eq. (8), and the scattering part of the source function is just the mean intensity J_x

$$\sigma(x, \mu) = \kappa_e, \quad S_{\text{sc}}(x, \mu) = J_x. \quad (39)$$

Compton scattering can be taken into account in the diffusion approximation using the Kompaneets equation [36] or using a fully relativistic angle-dependent redistribution function (RF) $R(x, \mu; x_1, \mu_1)$, which describes the probability that a photon with the dimensionless energy x_1 propagating in the direction corresponding to μ_1 is scattered to energy x and in the direction corresponding to μ [61, 37]. In our review, we consider the second case only. The function $R(x, \mu; x_1, \mu_1)$ is found by integrating over the azimuthal angle φ of the RF $R(x, x_1, \eta)$, which depends on the cosine of the angle between the directions of the photon propagation before and after scattering η

$$R(x, \mu; x_1, \mu_1) = \int_0^{2\pi} R(x, x_1, \eta) d\varphi, \quad (40)$$

$$\eta = \mu\mu_1 + \sqrt{1 - \mu^2} \sqrt{1 - \mu_1^2} \cos \varphi.$$

The RF depends on the depth s via the electron temperature and satisfies the relation

$$R(x_1, \mu_1; x, \mu) = R(x, \mu; x_1, \mu_1) \exp\left(\frac{x - x_1}{\Theta}\right), \quad (41)$$

which is the consequence of the detailed balance relation [62, 63]. Here,

$$\Theta = \frac{kT}{m_e c^2} \quad (42)$$

is the dimensionless electron temperature.

In this case, the electron scattering opacity is

$$\sigma(x, \mu) = \kappa_e \frac{1}{x} \int_0^\infty x_1 dx_1 \int_{-1}^1 d\mu_1 R(x_1, \mu_1; x, \mu) \left(1 + \frac{C I(x_1, \mu_1)}{x_1^3}\right), \quad (43)$$

where

$$C = \frac{1}{2m_e} \left(\frac{h}{m_e c^2}\right)^3, \quad (44)$$

and the scattering part of the source function is

$$S_{\text{sc}}(x, \mu) = \left(1 + \frac{C I(x, \mu)}{x^3}\right) x^2 \times \int_0^\infty \frac{dx_1}{x_1^2} \int_{-1}^1 d\mu_1 R(x, \mu; x_1, \mu_1) I(x_1, \mu_1). \quad (45)$$

The formal solution of the radiation transfer equation (35) is obtained using the short-characteristic method [64] in three angles in each hemisphere. The full solution is found with an accelerated Λ -iteration method (see details in Appendix of ref. [37]).

The radiation pressure acceleration g_{rad} is computed using the RF as

$$g_{\text{rad}} = \frac{dP_{\text{rad}}}{dm} = \frac{2\pi}{c} \frac{d}{dm} \int_0^\infty dx \int_{-1}^{+1} \mu^2 I(x, \mu) d\mu \quad (46)$$

$$= \frac{2\pi}{c} \int_0^\infty dx \int_{-1}^{+1} [\sigma(x, \mu) + k(x)] [I(x, \mu) - S(x, \mu)] \mu d\mu,$$

where the derivative with respect to m is replaced by the first moment of the radiation transfer equation (35). When the source functions and the opacities are isotropic, this expression is reduced to the standard definition

$$g_{\text{rad}} = \frac{4\pi}{c} \int_0^\infty [\sigma(x) + k(x)] H_x(m) dx. \quad (47)$$

These equations are completed by the energy balance equation

$$\int_0^\infty dx \int_{-1}^{+1} [\sigma(x, \mu) + k(x)] [I(x, \mu) - S(x, \mu)] d\mu = 0, \quad (48)$$

the ideal gas law

$$P = N_{\text{tot}} kT, \quad (49)$$

where N_{tot} is the number density of all particles, and the particle and charge conservation equations. The absorption opacity includes the free-free opacity as well as the bound-free transitions for all ions of the 15 most abundant chemical elements (H, He, C, N, O, Ne, Na, Mg, Al, Si, S, Ar, Ca, Fe, Ni) [59] using photoionization cross-sections from [65]. Opacities due to spectral lines can be considered for the cool NS models with coherent electron scattering using $\sim 25\,000$ spectral lines from the CHIANTI, Version 3.0, atomic database [66].

3.2.2 Solution method

Our version of the computer code ATLAS [67, 68] modified to deal with high temperatures [69, 60], is used to solve the above equations when the coherent electron scattering is considered. The code was further developed to account for Compton scattering using both the Kompaneets operator and the RF approach.

We can use various logarithmically equidistant frequency grids describing the whole NS spectral band for a given T_{eff} in our computations. If the spectral lines are taken into account, an extended grid with 20 000–40 000 points are used. The methods considering Compton scattering does not permit a large number of points, therefore, grids with 300–600 points is used. The grid of atmosphere depth layers consists of 98 depths m_i distributed equidistantly on a logarithmic scale from $10^{-6} - 10^{-8}$ to $m_{\text{max}} = 10^5 - 10^7 \text{ g cm}^{-2}$. The appropriate value of m_{max} is chosen to satisfy the inner boundary condition of the radiation transfer problem $J_x \approx B_x$. The outer boundary condition for the radiative transfer equation is the absence of any external radiation illuminating the atmosphere.

The first step of the calculations is the computation of an initial grey atmosphere model (see eq. 27) as well as of the opacities at all depths and all frequencies. The solution of the radiative transfer equation (35) was checked for the energy balance equation (48) together with the surface flux condition

$$4\pi \int_0^\infty H_x(m=0) dx = 4\pi H_0 = \sigma_{\text{SB}} T_{\text{eff}}^4. \quad (50)$$

The relative flux error

$$\varepsilon_H(m) = 1 - \frac{H_0}{\int_0^\infty H_x(m) dx}, \quad (51)$$

and the energy balance error

$$\varepsilon_A(m) = \frac{1}{2} \int_0^\infty dx \int_{-1}^{+1} [\sigma(x, \mu) + k(x)] [I(x, \mu) - S(x, \mu)] d\mu \quad (52)$$

were calculated as functions of depth. The temperature corrections were then evaluated using three different procedures. In the upper atmospheric layers, we used the integral Λ -iteration method. The temperature correction for a particular depth was found as

$$\Delta T_A = -\varepsilon_A(m) \left(\int_0^\infty \left[\frac{\Lambda_d(x) - 1}{1 - \alpha(x)\Lambda_d(x)} \right] k(x) \frac{dB_x}{dT} dx \right)^{-1}, \quad (53)$$

where $\alpha(x) = \sigma_{\text{CS}}(x)/(k(x) + \sigma_{\text{CS}}(x))$, and $\Lambda_d(x)$ is the diagonal matrix element of the Λ -operator. Here, $\sigma_{\text{CS}}(x)$ is the Compton scattering opacity averaged over the relativistic Maxwellian electron distribution (see eq. (A16) in [61]), which is equivalent to eq. (43) if one ignores the induced scattering), or just κ_e for the coherent electron scattering case. In the deep layers, we used the Avrett-Krook flux correction based on the relative flux error $\varepsilon_H(m)$. Finally, the third procedure was the surface correction based on the emergent flux error (see ref. [67] for a detailed description of the methods).

The iteration procedure is repeated until the relative flux error gets lower than 0.1% and the relative flux derivative error gets smaller than 0.01%. As a result, we obtain a self-consistent NS model atmosphere, together with the emergent spectrum of radiation. We note that this accuracy is unachievable for luminous models with $g_{\text{rad}} \approx g$. These models can have larger relative flux errors, up to 2–3%.

4 Applications to the real objects

Below, we present the results of NS model atmospheres applications to the real X-ray sources with NSs. We consider two classes of objects. The first class are thermally emitting NSs in the centers of the supernova remnants which do not show any evidence of accretion and of strong magnetic field. They are referred to as central compact objects (CCOs). The second class is comprised by X-ray bursting NSs in low-mass X-ray binaries.

4.1 Central compact objects in supernova remnants

The first point-like soft X-ray sources in the centers of some supernova remnants were assigned into a separate group of the NSs (CCOs) after the launch of the *Chandra* X-ray observatory [70, 71]. These sources have thermal spectra ($kT_{\text{BB}} \sim 0.2 - 0.6$ keV) and relatively low luminosities ($L_{\text{x}} \sim 10^{33} - 10^{34}$ erg s $^{-1}$). They have not been detected in any other electromagnetic wavelength range, from radio to γ -rays [72]. Currently, eight confirmed CCOs are known and three sources are considered to be CCO candidates (see Table 1 of [73]). Many of the CCOs have relatively good distance estimates, which is important for measuring the NS radii [70, 71, 73].

The CCO in Cas A is especially interesting. As mentioned in the Introduction, the carbon atmosphere has to be assumed to reconcile the derived size of the emitting region with that of a canonical NS [16]. Recently, the X-ray spectrum of another CCO situated near the center of the supernova remnant shell HESS J1731–347 (aka XMMU 1732), was obtained with the observatory *XMM-Newton* with a total exposure time ~ 100 ksec. The source is most probably located in the Scutum-Crux arm (~ 3 kpc) with the corresponding lower limit for the distance of ~ 3.2 kpc [74] derived on the basis of the X-ray absorption pattern and the absorbing column densities based on CO observations. The source spectrum is also well described by the carbon atmosphere model [21, 22].

We computed an extended grid of carbon NS model atmospheres to analyze X-ray spectra of this CCO. The models are computed for 9 values of surface gravity $\log g$, from 13.7 to 14.9 with a step of 0.15, which cover most of the realistic NS equations-of-state for a wide range of NS masses. For every value of $\log g$, we computed 61 models with T_{eff} from 1 to 4 MK with a step of 0.05 MK. This grid is available in form of an XSPEC model <http://heasarc.gsfc.nasa.gov/xanadu/xspec/models/carbatm.html>.

We assume that the carbon atmosphere covers the entire NS located at a distance D and used the direct fitting method (see eq. 1). The NS mass M and radius R are the fitting parameters, and they can be easily translated to the gravitational redshift z and the surface gravity g using eqs. (3) and (5). During a fit, the model spectra are interpolated between the grid values of T_{eff} and $\log g$. The resulting model spectrum is compared to the observed one

$$F_E = \frac{\mathcal{F}_{E(1+z)}(T_{\text{eff}}, g)}{1+z} \frac{R^2}{D^2}. \quad (54)$$

Here and later, we use the photon energy $E = h\nu$ instead of frequency ν to describe the X-ray observations. The distance D is formally a free parameter, but it can be fixed to obtain a useful confidence region in the $M - R$ plane. The model is multiplied by a component accounting for the interstellar photoelectric absorption characterized by the equivalent column density of hydrogen atoms N_{H} .

We thus performed our spectral fitting for the fixed distance of 3.2 kpc using blackbody, pure carbon and hydrogen model atmospheres. Both types of atmosphere models

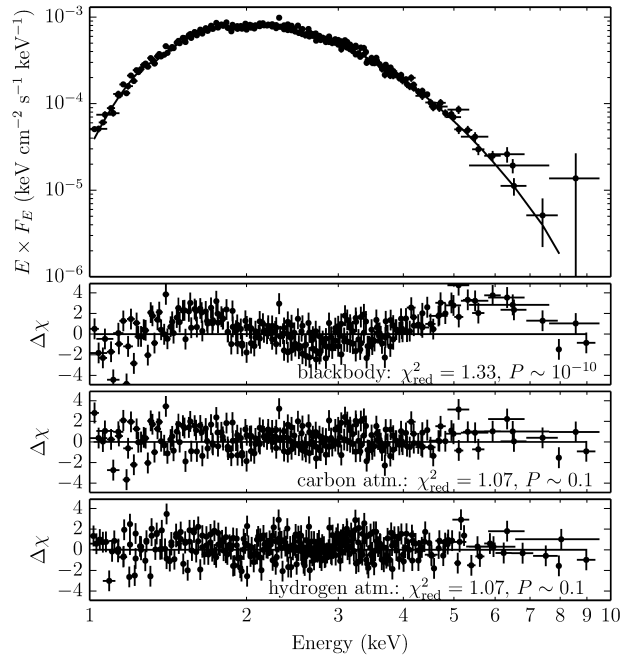


Fig. 11. The combined *XMM-Newton* spectrum (all three EPIC cameras) of the CCO in HESS J1731–347 from the three available observations fitted with a carbon atmosphere model (top panel) and the fit residuals for the blackbody, the carbon atmosphere, and the hydrogen atmosphere models (the lower three panels from top to bottom). The null-hypothesis probabilities (P -values) yielded by the χ^2 -fits are indicated. The blackbody model leads to a statistically unacceptable fit. From ref. [22].

provide a good fit to the data (fig. 11). The best-fit parameters obtained for the carbon atmosphere models are $M = 1.55^{+0.28}_{-0.24} M_{\odot}$, $R = 12.4^{+0.9}_{-2.2}$ km, $T_{\text{eff}} = 2.24^{+0.39}_{-0.13}$ MK, and $T_{\text{eff},\infty} = 1.78^{+0.04}_{-0.02}$ MK. The χ^2 confidence regions in the $M - R$ plane (50, 68, and 90% levels) are shown in fig. 12. The hydrogen models give unreasonably small M and R .

Unfortunately, strong interstellar absorption makes it difficult to directly observe carbon photoionization edges and the spectral lines, which are predicted by the atmosphere model. Potentially, their detection can give a possibility to determine the gravitational redshift, but long exposure times (up to a million second) might be needed for that. The problem might be even more severe if the magnetic field on the surface of the CCO in HESS J1731–347 is not as small as assumed, but above $10^{10} - 10^{11}$ G. The magnetic field would shift the ionization energies as well as the energies of the spectral lines, making direct determination of the gravitational redshift impossible. Furthermore, presently there are no magnetized carbon model atmospheres available, and we cannot predict how the magnetic field affects the fits.

The age of the CCO (~ 27 kyr) was estimated in ref. [75] assuming a distance of 3.2 kpc. The uncertainties of the age estimate are not well understood. We use a conservative range of 10–40 kyr. For larger distances, the age must be larger. The CCO is very hot for this age com-

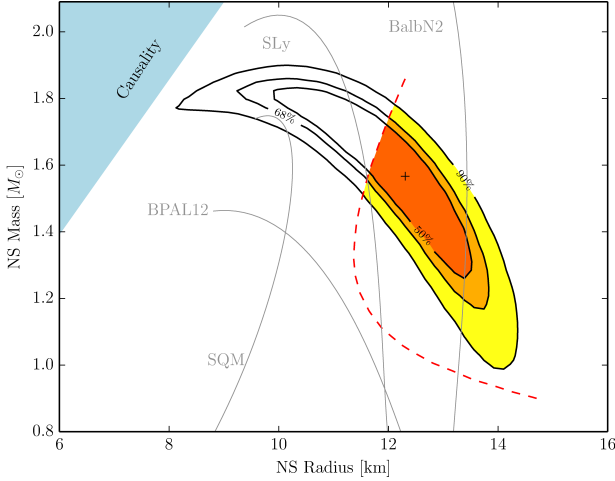


Fig. 12. The constraints on the mass and radius for the CCO in HESS J1731–347 assuming a distance of 3.2 kpc. The region on the right hand side of the red dashed curve is allowed by the cooling theory assuming a NS age of 27 kyr (see text for details). From ref. [22].

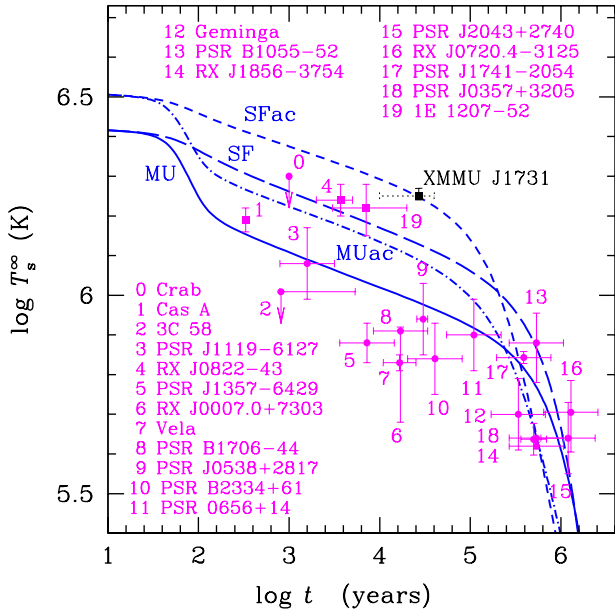


Fig. 13. The effective surface temperatures or upper limits for a number of cooling isolated NSs including CCO in HESS J1731–347 (marked as XMMU 1731) versus their ages (data points) compared with four theoretical cooling curves for a $1.5 M_{\odot}$ star. The plot contains four CCOs with reliable temperature measurements (labeled with squares). For HESS J1731–347, the dashed error bar indicates a conservative range of 10–40 kyr adopted for the NS age. MU refers to a non-superfluid star with a heat blanket made of iron; SF corresponds to a star with strong proton superfluidity in the core and the same heat blanket; MUac and SFac refer, respectively, to the same models as MU and SF but with a fully carbon heat blanketing envelope (see text for details). From ref. [22].

pared to other isolated cooling NSs (see a $T_s^{\infty} - t$ diagram in fig. 13, where t is the estimated/measured age of the objects and $T_s^{\infty} \equiv T_{\text{eff},\infty}$ is the apparent effective surface temperature). This unusual property of the CCO in HESS J1731–347 provides additional constraints on the NS parameters using the current NS cooling theory (see details and references in ref. [22]). The CCO must have a very low neutrino luminosity and an unusually heat-transparent blanketing envelope for the observed slow cooling down. The required low neutrino luminosity can be realized in a star with strong proton superfluidity in the core (where neutrino emission is produced by neutron-neutron collisions). High heat transparency can be provided by the presence of a sufficient amount of carbon in the heat blanketing envelope. For a star’s age of 27 kyr, the heat blanket should contain the maximum amount of carbon, $\Delta M \sim 10^{-8} M_{\odot}$.

The theoretical cooling curves depend (although not very strong) on M and R for the observed T_s^{∞} . Therefore, the observed T_s^{∞} and age cannot be reconciled for certain M and R , where the theoretical cooling curve goes below the inferred T_s^{∞} even at the extreme parameters of the cooling regulators. These values of M and R can be treated as *forbidden* by the cooling theory which gives additional constraints on M and R . Under the assumptions described in detail in ref. [22], the cooling theory mostly eliminates the range of small $R \leq 12$ km (see fig. 12). Recently, more sophisticated cooling theory was used for this kind of limitation [76], but this analysis almost did not change the basic conclusions.

4.2 X-ray bursting neutron stars in low-mass X-ray binaries

X-ray bursting NSs are members of close binary systems with the secondary low-mass star overfilling its Roche lobe (so called low-mass X-ray binaries, LMXBs) with a relatively low accretion rate, see reviews in ref. [24, 38]. X-ray bursts are the observational manifestation of thermonuclear flashes occurring at the bottom of freshly accreted matter on the NS surface. Some of them can be so powerful that the X-ray burst luminosity L reaches the Eddington limit L_{Edd} leading to the expansion of the photosphere as measured by an increase of blackbody normalization K . Such photospheric radius expansion (PRE) bursts provide important information about the NS compactness from the observed Eddington flux and the maximum effective temperature of the NS surface [25, 29, 30].

The observed spectra of X-ray bursts are well-fitted by a blackbody [38]

$$F_E = \pi B_E(T_{\text{BB}}) K_{\text{BB}} = \pi B_E(T_{\text{BB}}) \frac{R_{\text{BB}}^2}{D^2}. \quad (55)$$

In fact, the emergent spectra are close to the diluted blackbody spectra because of strong photon-electron interaction in hot NS atmospheres, as it was described above

$$\mathcal{F}_E \approx f_c^{-4} \pi B_E(T_c = f_c T_{\text{eff}}). \quad (56)$$

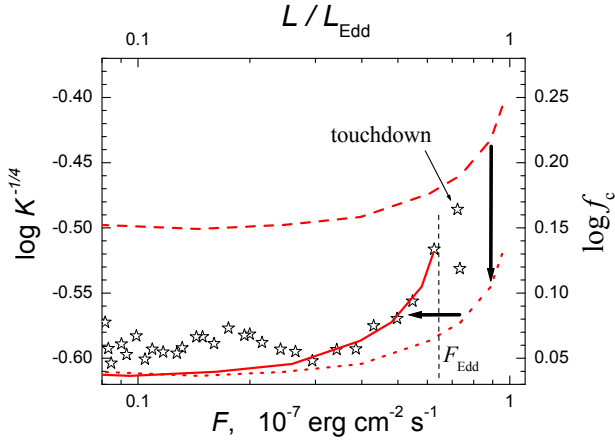


Fig. 14. Scheme of fitting of the observed dependence $K_{\text{BB}}^{-1/4} - F_{\text{BB}}$ (stars) by the computed dependence $f_c - l$ (dashed curve). From ref. [36].

Recently, we suggested a new cooling tail method for NS mass and radius determination using X-ray bursts with PRE [36,40]. This method is based on the fact that the observed normalization K_{BB} of an isolated passively cooling NS is proportional to the dilution factor f_c^{-4} only

$$K_{\text{BB}} = \frac{R^2(1+z)^2}{f_c^4 D^2}. \quad (57)$$

This conclusion can be easily obtained using this chain of reasoning for the observed bolometric flux

$$\sigma_{\text{SB}} T_{\text{BB}}^4 K_{\text{BB}} = \sigma_{\text{SB}} T_{\text{eff},\infty}^4 \frac{R^2(1+z)^2}{D^2}, \quad (58)$$

where the observed blackbody temperature can be expressed as

$$T_{\text{BB}} = \frac{T_c}{1+z} = \frac{f_c T_{\text{eff}}}{1+z} = f_c T_{\text{eff},\infty}. \quad (59)$$

The approximation presented by eq. (56) conserves bolometric flux

$$\mathcal{F} = \frac{1}{f_c^4} \sigma_{\text{SB}} T_c^4 = \sigma_{\text{SB}} T_{\text{eff}}^4, \quad (60)$$

therefore, we find the relation given by eq. (57) between the observed normalization K_{BB} and the computed colour correction factor f_c .

As mentioned above, the colour correction factor f_c depends mainly on the relative NS luminosity $l = L/L_{\text{Edd}}$. Therefore, the observed normalization K_{BB} has to depend on the observed bolometric flux F_{BB} in the same way as the computed f_c^{-4} depends on l . Therefore, we can fit the observed dependence $K_{\text{BB}}^{-1/4} - F_{\text{BB}}$ with the computed one $f_c - l$ in the cooling phase of the burst (see fig. 14) and obtain two fitting parameters

$$A = \left(\frac{R(1+z)}{D} \right)^{-1/2}, \quad \text{so that} \quad K_{\text{BB}}^{-1/4} = f_c A, \quad (61)$$

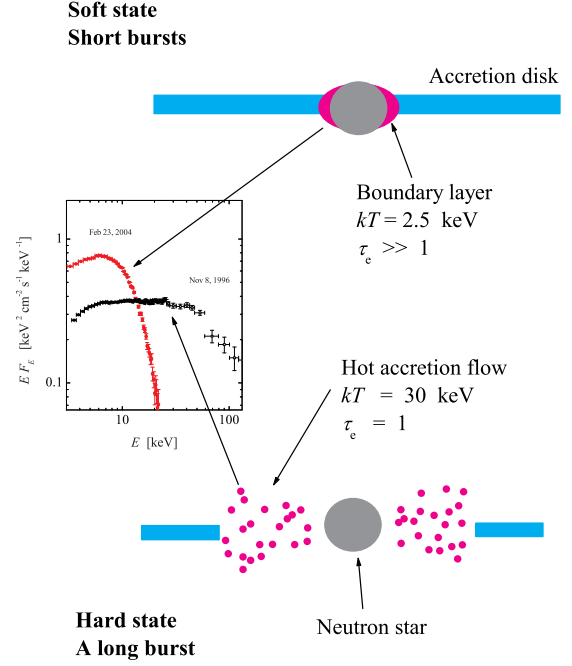


Fig. 15. A sketch of accretion structures around the NS in a LMXB in the soft and hard persistent states together with the corresponding persistent X-ray spectra before two PRE bursts in 4U 1724–307 [40].

and the observed Eddington flux

$$F_{\text{Edd}} = \frac{L_{\text{Edd},\infty}}{4\pi D^2} = \frac{GM}{\kappa_e D^2} \frac{1}{1+z}. \quad (62)$$

They can be combined to the observed Eddington temperature which is independent of D

$$T_{\text{Edd},\infty} = A \left(\frac{F_{\text{Edd}}}{\sigma_{\text{SB}}} \right)^{1/4} = 9.81 A' F_{\text{Edd},-7}^{1/4} \text{ keV}, \quad (63)$$

where $F_{\text{Edd},-7} = F_{\text{Edd}}/10^{-7} \text{ erg s}^{-1} \text{ cm}^{-2}$, and the normalized fitting parameter $A' = (R_{\infty}[\text{km}]/D_{10})^{-1/2}$ with $D_{10} = D/10 \text{ kpc}$. The Eddington temperature $T_{\text{Edd},\infty}$ found from observation determines a specific curve in the $M - R$ plane (see fig. 1), which allows the NS radius to be evaluated, as NS masses are in a range $1.2 - 2 M_{\odot}$.

The described method can be applied to the NS mass and radius measurements if our assumption of a passively cooling “isolated” NS in empty space as a model of an X-ray bursting NS during cooling phase is correct. In reality, X-ray bursting NSs are accreting NSs with the accretion discs around them. It is well known that LMXBs can have two qualitatively different persistent spectral states: the soft/high state and the hard/low state (see fig. 15). The luminosities of LMXBs in the soft states are relatively high ($\sim 0.1 L_{\text{Edd}}$) and their spectra can be composed of the soft ($kT < 1 \text{ keV}$) and the hard ($kT \sim 2 - 2.5 \text{ keV}$) components [77,78]. These components likely correspond to the optically thick accretion disc and to the optically

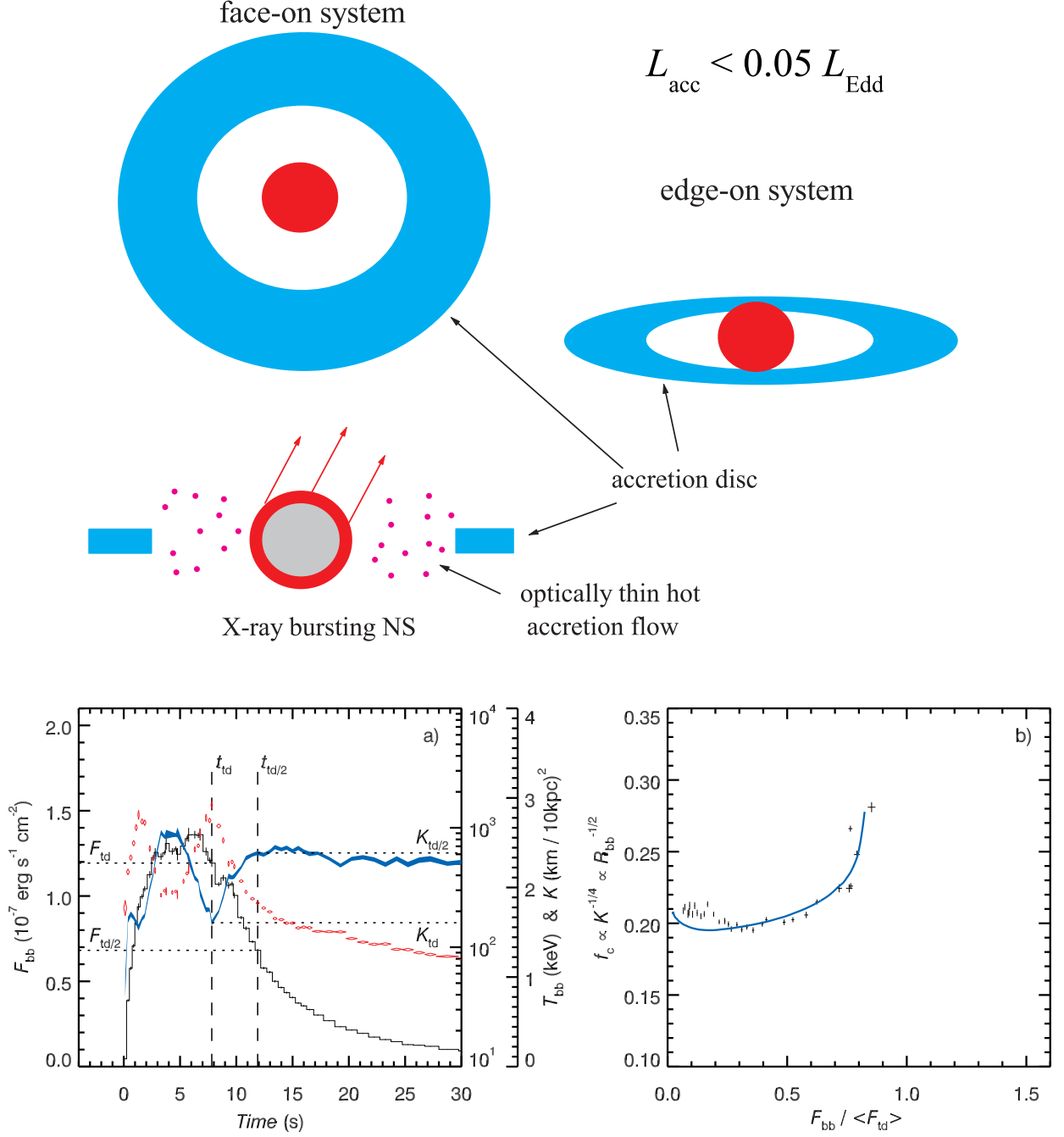


Fig. 16. Top panel: A sketch of the radial cross-section of accretion structures around the NS in the hard persistent state of LMXBs together with the projections on the sky for low (face-on) and high (edge-on) inclination systems. Bottom panel: The time resolved spectroscopy of a PRE X-ray burst from 4U 1608–52 in the hard persistent state taken from ref. [82]. In the left panel, the black line shows the bolometric flux F_{BB} (left-hand Y-axis). The blue ribbon shows the 1σ limits of the black body normalisation $K_{\text{BB}} = (R_{\text{BB}}[\text{km}]/D_{10})^2$ (inner right-hand y-axis). The red diamonds show the 1σ errors for black body temperature T_{BB} in keV (outer right-hand y-axis). The first black vertical dashed line marks the time of touchdown t_{td} and the second vertical dashed line to the right shows the time $t_{\text{td}/2}$ when F_{BB} has decreased to one half of the touchdown flux. The corresponding F_{BB} and K_{BB} -values at these times F_{td} , $F_{\text{td}/2}$, K_{td} and $K_{\text{td}/2}$ are marked with dotted lines. The right panel shows the relationship between the inverse square root of the black body radius (proportional to the colour-correction factor f_c) and the black body flux F_{BB} that is scaled using the mean touchdown flux $\langle F_{\text{td}} \rangle$. The blue line is the model prediction for a pure hydrogen NS atmosphere with a surface gravity of $\log g = 14.3$ [37].

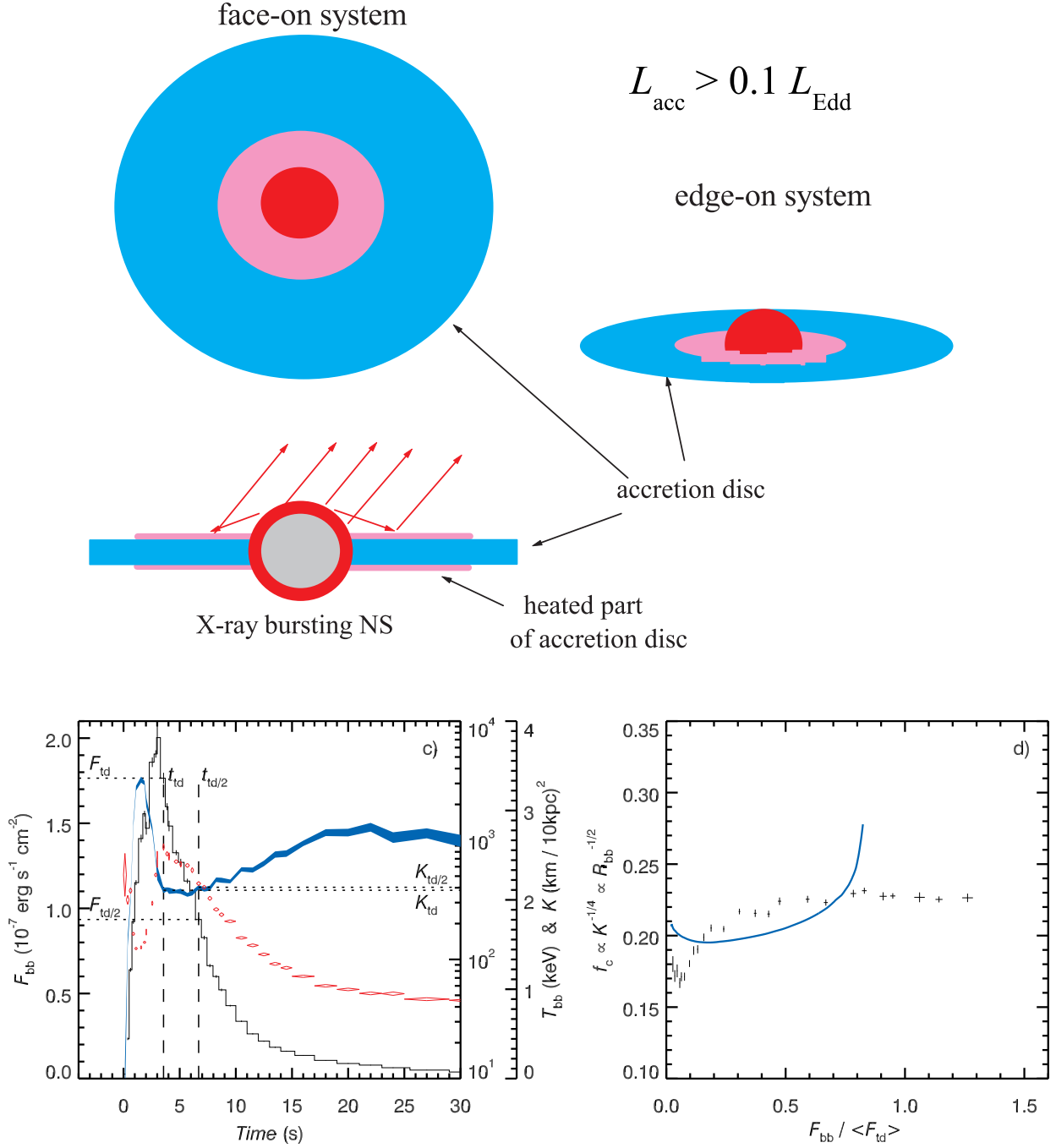


Fig. 17. Top panel: A scheme of the radial cross-section of the accretion structures around the NS in the soft persistent state of a LMXB together with the projections on the sky for low (face-on) and high (edge-on) inclination systems. Bottom panel: The same as in fig. 16, but for the PRE burst of 4U 1608–52 in the soft persistent state. From ref. [82].

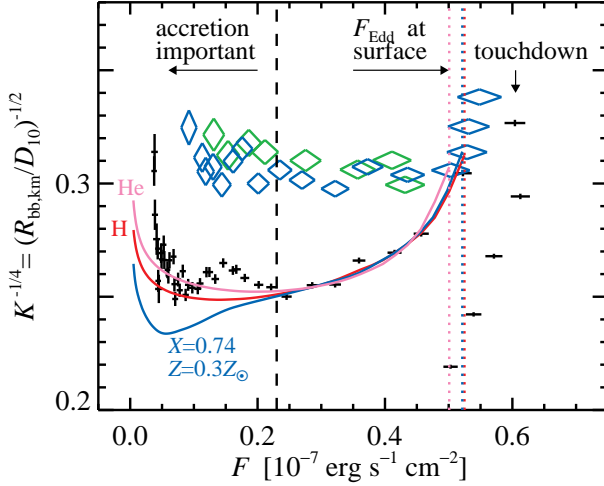


Fig. 18. A comparison of the X-ray burst data for 4U 1724–307 with the theoretical models of the NS atmosphere. The crosses indicate the observed $K_{\text{BB}}^{-1/4} - F_{\text{BB}}$ dependence for a PRE burst in the hard persistent state, while diamonds represent two PRE bursts in the soft persistent state. The solid curves correspond to the three best-fit theoretical models of various chemical compositions. From ref. [40].

thick boundary layer between the accretion disc and the NS surface [79,69]. Low luminosity LMXBs ($L \sim 0.01 - 0.05 L_{\text{Edd}}$) show hard X-ray spectra described by emission models of optically thin ($\tau_e \sim 1$) hot ($kT \sim 20 - 30$ keV) thermal Comptonization. This means that the spectra are formed by multiple Compton scattering of the soft photons on the hot plasma electrons [80]. Therefore, optically thick discs do not exist in those states. They are transformed to the geometrically thick optically thin hot accretion flows, most probably due to the accretion disc evaporation [81]. Intermediate spectral states with various contributions of the optically thick boundary layer, the hot optically thin accretion flow as well as the standard accretion disc to the observed spectra are also observed.

It seems that the optically thin accretion flow could affect X-ray burst flux less significantly compared to the optically thick disc. Moreover, the hot flow could be completely blown away by a PRE burst. Therefore, we can expect that the best accordance of the real X-ray bursting NS with the ideal model occurs in PRE burst happening in the hard persistent state during the phase between the touchdown and a point when the accretion starts again. The touchdown point (t_{td}) is the moment of the PRE X-ray burst with the maximum observed blackbody temperature T_{BB} and the minimum value of the normalization K_{BB} [38]. It is commonly accepted that the NS photospheric size does not change after this moment, and the corresponding bolometric flux F_{td} is close to the observed Eddington flux. Indeed, there is a number of PRE X-ray bursts in the hard persistent states, which demonstrate a theoretically predicted dependences $K_{\text{BB}}^{-1/4} - F_{\text{BB}}$ in these X-ray burst phases, see, e.g., the PRE bursts from 4U 1608–52 (fig. 16) [41,82,42]. Therefore, we can use this kind of PRE bursts to measure NS masses and radii.

On the other hand, the optically thick accretion disc has to affect the observed flux and spectrum of an X-ray burst significantly. It reflects the X-ray burst flux and blocks part of the bursting NS in high inclination systems (fig. 17). This is a well known problem of radiation anisotropy of X-ray bursts [24]

$$F_E = \xi_b^{-1} \frac{L_{E,\infty}}{4\pi D^2}. \quad (64)$$

The anisotropy coefficient can be expressed with a simple formula [83]

$$\xi_b^{-1} = \frac{1}{2} + \cos i, \quad (65)$$

where i is the inclination angle, i.e. the angle between the accretion disc axis and the line of sight. According to this approximation, F_{td} for a PRE burst in the soft persistent state can be one and a half times higher than F_{td} for a PRE burst in the hard persistent state in face-on systems ($\cos i \approx 1$). In fig. 17 (bottom panel) an example of such a PRE burst in 4U 1608–52 during the soft persistent state is shown. Indeed, its touchdown flux is about 1.5 times larger than the touchdown flux of other bursts during the hard state. It is thus possible that 4U 1608–52 is a face-on system. We also note that the dependence $K_{\text{BB}}^{-1/4} - F_{\text{BB}}$ is flat for this burst and its behaviour is inconsistent with the predictions made on the base of eq. (57). It means that this equation cannot be applied to the PRE bursts in the soft persistent state because of the accretion disc (whose effect is not completely understood) and the influence of the boundary layer. Nevertheless, the PRE X-ray bursts occurring in the soft persistent states with the flat $K_{\text{BB}}^{-1/4} - F_{\text{BB}}$ dependences have been widely used to determine NS parameters [84,85,86], leading obviously to strongly biased results.

LMXB 4U 1724–307 is another example to study the difference between the soft and hard state bursts (see fig. 18 and [40]). The dependence $K_{\text{BB}}^{-1/4} - F_{\text{BB}}$ for the PRE burst in the hard persistent state can be well fitted with the theoretical $f_c - l$ dependence. In the same figure, the dependences $K_{\text{BB}}^{-1/4} - F_{\text{BB}}$ for two other PRE bursts in the soft persistent states are shown. They are also flat like in 4U 1608–52, but the corresponding blackbody normalization K_{BB} is two times smaller than that for the PRE in the hard persistent state. Unlike 4U 1608–52, this source has similar maximum fluxes in the PRE bursts happening during the soft and in the hard persistent states. We speculate that 4U 1724–307 might be a highly inclined system, and the accretion disc blocks part of the NS in the soft persistent state, whereas the reflected flux has a negligible contribution to the total luminosity. It is clear that the properties of the PRE bursts depend strongly on the spectral state of the persistent emission before the burst [41,82].

We applied the cooling tail method to the PRE bursts of two LMXBs, 4U 1724–307 [40] and 4U 1608–52 [41], observed by the *RXTE* during their hard states. The obtained allowed regions in the $M - R$ plane for these NSs are presented in figs. 19 and 20. There are two main sources

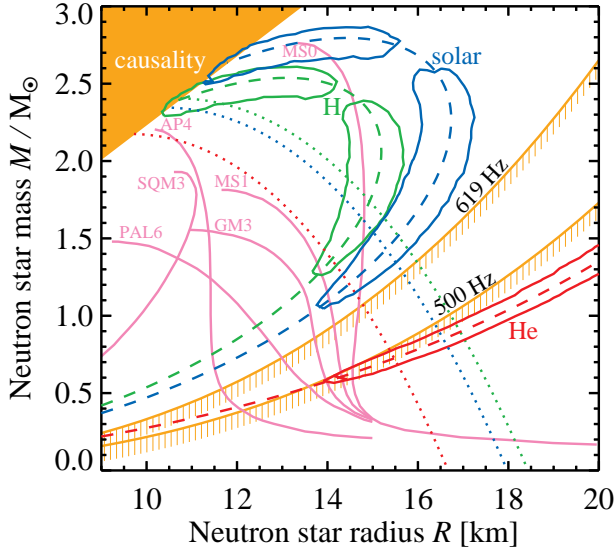


Fig. 19. The mass-radius constraints from a hard-state PRE burst of 4U 1724–307 for three chemical compositions: green for pure hydrogen, blue for the solar H/He ratio and subsolar metal abundance $Z = 0.3Z_{\odot}$, and red for pure helium assuming a flat distribution of the distance between 5.3 and 7.7 kpc with Gaussian tails of $1\sigma=0.6$ kpc. The constraints are shown by contours (90% confidence level). The mass-radius relations for several equations of state of neutron and strange star matter are shown with solid pink curves. The brown solid curves in the lower right region correspond to the mass-shedding limit and delineate the zone forbidden for the NS in 4U 1724–307, if it had a rotational frequency of 500 or 619 Hz. The dotted curves correspond to the best-fit parameter A for the distance to the source of 5.3 kpc. From ref. [40].

of uncertainties: the atmosphere chemical composition and the distance. Hydrogen rich atmospheres give reasonable NS radii, 13–16 km, while helium rich atmospheres are excluded for both NSs because they give too large (> 20 km) radii for $1.5 M_{\odot}$ mass. We note the solutions in figs. 19 and 20 are divided into two parts and the region near the line $R = 4GM/c^2$ is formally not allowed because of the degeneracy in the transformation from (F_{Edd}, A) to (M, R) [87]. The Bayesian analysis assuming flat priors in M and R instead of F_{Edd} and A is free from this disadvantage, and the solutions close to $R = 4GM/c^2$ also become possible [87, 42].

Nevertheless, the obtained NS radii appear somewhat larger than the radius of the CCO in HESS 1731–347 and the expected NS radii from modern equation of states in NS cores [88]. A possible reason for this is a rapid rotation of the investigated NSs. The measured spin frequency of the NS in 4U 1608–52 is 620 Hz. Such a rapid rotation distorts the NS shape making the equatorial radius larger than the polar one [89]. As a result, an equivalent apparent radius of a rapidly rotating NS becomes significantly larger than the radius of the non-rotating NS of the same mass [90]. Additionally, the combination of the shape distortion and the centrifugal force affects the surface gravity making it a function of the latitude, with the effective gravity being reduced at the equator. This

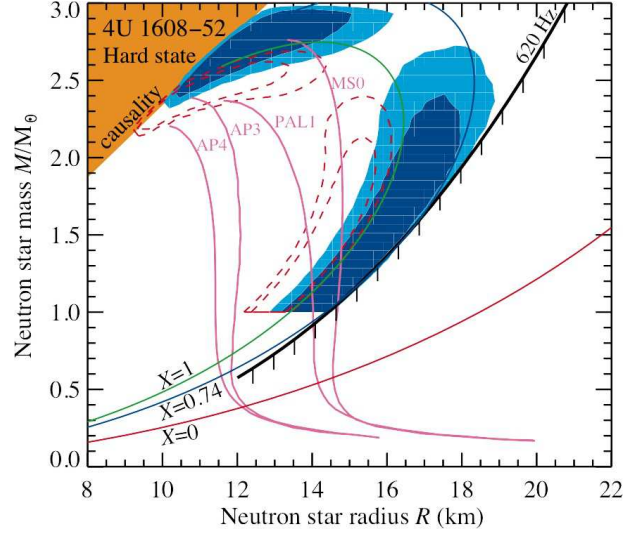


Fig. 20. The mass-radius constraints from the PRE bursts of 4U 1608–52 in the hard persistent state assuming $M > 1.0 M_{\odot}$, distance 5.8 ± 2.0 kpc, and a hydrogen rich atmosphere ($X > 0.74$). The dark and the light contours correspond to 68 and 90% confidence levels. The red dashed contours give constraints with different data selection. The mass shedding limit for a spin frequency of 620 Hz (measured in this source from coherent pulsations during some bursts) is marked by the black curve with downward ticks. The solid green, blue, and red curves marked with $X = 1$, $X = 0.74$, and $X = 0$ correspond to the best-fitting $T_{\text{Edd},\infty}$ assuming pure hydrogen, solar mix, and pure helium atmosphere compositions. The NS mass-radius relations for several equation of states that have the maximum possible masses $> 2 M_{\odot}$ are shown with thin pink curves. From ref. [41].

in turn results in the latitude dependence of the critical (Eddington) flux and reduction of the latitude-averaged critical luminosity compared to the Eddington limit for the non-rotating NS. Preliminary computations showed, that we can expect that the radius of a non-rotating NS can be 1–2 km smaller compared to the measured radius of the NS in 4U 1608–52. We finally note that our most recent analysis of the carefully selected sample of hard-state bursts from 4U 1702–429, SAX J1810.8–2609 and 4U 1724–307 produced NS radii in the range 10.5–12.8 km [42] which is consistent with the estimates coming from the HESS 1731–347 CCO.

5 Summary

We presented the basic ideas and methods allowing to measure NS masses and radii from the analysis of their broad band X-ray spectra. The model atmosphere spectra are the key ingredient of the methods. We qualitatively described the main features of the simplest NS model atmospheres together with the basic assumptions used for NS model atmosphere computations. Our review is limited to non-magnetic NSs because the construction of the magnetized NS model atmospheres is much more complicated

and is associated with a large number of uncertainties in the magnetized plasma opacities and with additional geometry problems [91].

There are two main effects making the model NS spectra harder than the blackbody spectra with the same effective temperature: (i) the decrease of the absorption opacity with the photon energy and (ii) the increase of the atmospheric temperature with depth. Due of these atmosphere properties, the emergent photons preferentially escape at higher energies where the atmosphere is more transparent. As a result, the emitting NS sizes derived from blackbody fits are significantly smaller than the actual NS radii. Accurate model atmospheres are necessary to take these differences correctly into account. The additional opaque spectral bands due to photoionization edges in the not fully ionized atmospheres force emergent photons to escape at even harder energies further increasing the deviation of the model atmosphere spectrum from the blackbody.

We also presented the previously published results of the NS mass and radius measurements using the model NS spectra for two types of X-ray sources: the CCO in supernova remnant HESS 1731–347 and X-ray bursting NSs in LMXBs, 4U 1724–307 and 4U 1608–52. The *XMM-Newton* spectrum of the first source was fitted with the carbon model atmosphere spectrum for the fixed distance of 3.2 kpc with an additional limitation obtained from the NS cooling theory for the assumed age of 10–40 kyr. The radius of 12–14 km and the mass of 1.2–1.7 M_{\odot} were obtained for this NS. The X-ray bursting NSs parameters were derived using a novel cooling tail method and the larger NS radii (>13 km for hydrogen rich atmospheres and NS masses 1.0–2 M_{\odot}) were obtained. The NS in 4U 1608–52 rotates rapidly with the spin frequency of 620 Hz. We thus suggest an unaccounted NS shape distortion to be the reason for this difference in the radii. The spin frequency of the NS in 4U 1724–307 is unknown, but it is also likely to be high and the same explanation is valid for this NS as well. On the other hand, our recent analysis of X-ray bursters from three LMXBs 4U 1702–429, SAX J1810.8–2609 and 4U 1724–307 show the radii in the range 10.5–12.8 km. These results favour a reasonably stiff equation of state of cold dense matter.

We thank J. Kajava, J. Nättilä, G. Pühlhofer, D. Yakovlev, G. G. Pavlov, A. Santangelo and other co-authors of the works used here for the successful collaborations. V.F.S. thanks DFG for financial support (grant WE 1312/48-1). J.P. acknowledges the Academy of Finland grant 268740.

References

1. P. Haensel, A.Y. Potekhin, D.G. Yakovlev, *Neutron Stars 1: Equation of State and Structure*, Vol. 326 of *Astrophysics and Space Science Library* (Springer, New York, 2007)
2. J.M. Lattimer, M. Prakash, *Phys. Rep.* **442**, 109 (2007), [arXiv:astro-ph/0612440](#)
3. F. Özel, *Reports on Progress in Physics* **76**(1), 016901 (2013), 1210.0916
4. F.M. Walter, S.J. Wolk, R. Neuhauser, *Nat* **379**, 233 (1996)
5. V.E. Zavlin, G.G. Pavlov, Y.A. Shibano, *A&A* **315**, 141 (1996), [arXiv:astro-ph/9604072](#)
6. M. Rajagopal, R.W. Romani, *ApJ* **461**, 327 (1996), [astro-ph/9510094](#)
7. V.E. Zavlin, in *Neutron Stars and Pulsars*, Vol. 357 of *Astrophysics and Space Science Library*, edited by W. Becker (Springer, New York, 2009), p. 181
8. C. Alcock, A. Illarionov, *ApJ* **235**, 534 (1980)
9. J.M. Hameury, J. Heyvaerts, S. Bonazzola, *A&A* **121**, 259 (1983)
10. E.F. Brown, L. Bildsten, P. Chang, *ApJ* **574**, 920 (2002), [astro-ph/0204102](#)
11. C.O. Heinke, G.B. Rybicki, R. Narayan, J.E. Grindlay, *ApJ* **644**, 1090 (2006), [arXiv:astro-ph/0506563](#)
12. S. Guillot, M. Servillat, N.A. Webb, R.E. Rutledge, *ApJ* **772**, 7 (2013), 1302.0023
13. A. Catuneanu, C.O. Heinke, G.R. Sivakoff, W.C.G. Ho, M. Servillat, *ApJ* **764**, 145 (2013), 1301.3768
14. V.E. Zavlin, G.G. Pavlov, J. Trumper, *A&A* **331**, 821 (1998), [astro-ph/9709267](#)
15. G.G. Pavlov, G.J.M. Luna, *ApJ* **703**, 910 (2009), 0905.3190
16. W.C.G. Ho, C.O. Heinke, *Nat* **462**, 71 (2009), 0911.0672
17. C.O. Heinke, W.C.G. Ho, *ApJ* **719**, L167 (2010), 1007.4719
18. P.S. Shternin, D.G. Yakovlev, C.O. Heinke, W.C.G. Ho, D.J. Patnaude, *MNRAS* **412**, L108 (2011), 1012.0045
19. K.G. Elshamouty, C.O. Heinke, G.R. Sivakoff, W.C.G. Ho, P.S. Shternin, D.G. Yakovlev, D.J. Patnaude, L. David, *ApJ* **777**, 22 (2013), 1306.3387
20. B. Posselt, G.G. Pavlov, V. Suleimanov, O. Kargaltsev, *ApJ* **779**, 186 (2013), 1311.0888
21. D. Klochkov, G. Pühlhofer, V. Suleimanov, S. Simon, K. Werner, A. Santangelo, *A&A* **556**, A41 (2013), 1307.1230
22. D. Klochkov, V. Suleimanov, G. Pühlhofer, D.G. Yakovlev, A. Santangelo, K. Werner, *A&A* **573**, A53 (2015), 1410.1055
23. V.F. Suleimanov, D. Klochkov, G.G. Pavlov, K. Werner, *ApJS* **210**, 13 (2014), 1311.6037
24. W.H.G. Lewin, J. van Paradijs, R.E. Taam, *Space Science Reviews* **62**, 223 (1993)
25. T. Ebisuzaki, *PASJ* **39**, 287 (1987)
26. J. van Paradijs, W.H.G. Lewin, *A&A* **172**, L20 (1987)
27. M. Sztajno, M.Y. Fujimoto, J. van Paradijs, W.D. Vacca, W.H.G. Lewin, W. Penninx, J. Trumper, *MNRAS* **226**, 39 (1987)
28. M.Y. Fujimoto, M. Gottwald, *MNRAS* **236**, 545 (1989)
29. E. Damen, E. Magnier, W.H.G. Lewin, J. Tan, W. Penninx, J. van Paradijs, *A&A* **237**, 103 (1990)
30. J. van Paradijs, T. Dotani, Y. Tanaka, T. Tsuru, *PASJ* **42**, 633 (1990)
31. R.A. London, R.E. Taam, W.M. Howard, *ApJ* **306**, 170 (1986)
32. I.I. Lapidus, R.A. Syunyaev, L.G. Titarchuk, *Soviet Astronomy Letters* **12**, 383 (1986)
33. V.E. Zavlin, Y.A. Shibano, *Sov. Astr.* **35**, 499 (1991)
34. G.G. Pavlov, I.A. Shibano, V.E. Zavlin, *MNRAS* **253**, 193 (1991)
35. J. Madej, *ApJ* **376**, 161 (1991)

36. V. Suleimanov, J. Poutanen, K. Werner, *A&A* **527**, A139 (2011), 1009.6147
37. V. Suleimanov, J. Poutanen, K. Werner, *A&A* **545**, A120 (2012), 1208.1467
38. D.K. Galloway, M.P. Muno, J.M. Hartman, D. Psaltis, D. Chakrabarty, *ApJS* **179**, 360 (2008), [arXiv:astro-ph/0608259](#)
39. J. Nättilä, V.F. Suleimanov, J.J.E. Kajava, J. Poutanen, *A&A* **581**, A83 (2015), 1507.01525
40. V. Suleimanov, J. Poutanen, M. Revnivtsev, K. Werner, *ApJ* **742**, 122 (2011)
41. J. Poutanen, J. Nättilä, J.J.E. Kajava, O.M. Latvala, D.K. Galloway, E. Kuulkers, V.F. Suleimanov, *MNRAS* **442**, 3777 (2014), 1405.2663
42. J. Nättilä, A.W. Steiner, J.J.E. Kajava, V.F. Suleimanov, J. Poutanen, *ArXiv e-prints* (2015), 1509.06561
43. A.D. Kaminker, G.G. Pavlov, Y.A. Shibano, V.G. Kurt, A.S. Smirnov, V.M. Shamolin, I.F. Kopaeva, E.K. Sheffer, *A&A* **220**, 117 (1989)
44. A. Majczyna, J. Madej, *Acta Astr.* **55**, 349 (2005)
45. G.B. Rybicki, A.P. Lightman, *Radiative processes in astrophysics* (Wiley-Interscience, New York, 1979)
46. S.L. Shapiro, S.A. Teukolsky, *Black holes, white dwarfs, and neutron stars: The physics of compact objects* (Wiley-Interscience, New York, 1983)
47. A.Y. Potekhin, *Physics Uspekhi* **57**, 735 (2014), 1403.0074
48. R.E. Rutledge, L. Bildsten, E.F. Brown, G.G. Pavlov, V.E. Zavlin, *ApJ* **514**, 945 (1999), [astro-ph/9810288](#)
49. M. Servillat, C.O. Heinke, W.C.G. Ho, J.E. Grindlay, J. Hong, M. van den Berg, S. Bogdanov, *MNRAS* **423**, 1556 (2012), 1203.5807
50. A.M. Juett, D. Psaltis, D. Chakrabarty, *ApJ* **560**, L59 (2001), [astro-ph/0108102](#)
51. D. Mihalas, *Stellar atmospheres, 2nd ed.* (W. H. Freeman and Co., San Francisco, 1978)
52. T. Rauch, V. Suleimanov, K. Werner, *A&A* **490**, 1127 (2008), 0809.2170
53. D.G. Hummer, D. Mihalas, *ApJ* **331**, 794 (1988)
54. I. Hubeny, D.G. Hummer, T. Lanz, *A&A* **282**, 151 (1994)
55. V.E. Zavlin, G.G. Pavlov, Y.A. Shibano, *Astronomical and Astrophysical Transactions* **4**, 307 (1994)
56. J. Frank, A. King, D.J. Raine, *Accretion Power in Astrophysics* (Cambridge University Press, Cambridge, 2002)
57. M.J. Seaton, Y. Yan, D. Mihalas, A.K. Pradhan, *MNRAS* **266**, 805 (1994)
58. B. Paczynski, *ApJ* **267**, 315 (1983)
59. A.A. Ibragimov, V.F. Suleimanov, A. Vikhlinin, N.A. Sakhibullin, *Astronomy Reports* **47**, 186 (2003)
60. V. Suleimanov, K. Werner, *A&A* **466**, 661 (2007), [arXiv:astro-ph/0702407](#)
61. J. Poutanen, R. Svensson, *ApJ* **470**, 249 (1996), [arXiv:astro-ph/9605073](#)
62. G.C. Pomraning, *The equations of radiation hydrodynamics* (Pergamon Press, Oxford, 1973)
63. D.I. Nagirner, J. Poutanen, *Astrophysics and Space Physics Reviews* **9**, 1 (1994)
64. G.L. Olson, P.B. Kunasz, *JQSRT* **38**, 325 (1987)
65. D.A. Verner, D.G. Yakovlev, *A&AS* **109**, 125 (1995)
66. K.P. Dere, E. Landi, H.E. Mason, B.C. Monsignori Fossi, P.R. Young, *A&AS* **125**, 149 (1997)
67. R.L. Kurucz, *SAO Special Report* **309** (1970)
68. R. Kurucz, *ATLAS9 Stellar Atmosphere Programs and 2 km/s grid*. Kurucz CD-ROM No. 13. Cambridge, Mass.: Smithsonian Astrophysical Observatory, 1993. **13** (1993)
69. V. Suleimanov, J. Poutanen, *MNRAS* **369**, 2036 (2006), [arXiv:astro-ph/0601689](#)
70. G.G. Pavlov, D. Sanwal, G.P. Garmire, V.E. Zavlin, in *Neutron Stars in Supernova Remnants*, edited by P.O. Slane, B.M. Gaensler (2002), Vol. 271 of *ASP Conf. Ser.*, p. 247, [astro-ph/0112322](#)
71. G.G. Pavlov, D. Sanwal, M.A. Teter, in *Young Neutron Stars and Their Environments*, Vol. 218 of *IAU Symposium*, edited by F. Camilo, B.M. Gaensler (2004), p. 239, [astro-ph/0311526](#)
72. E.V. Gotthelf, J.P. Halpern, in *40 Years of Pulsars: Millisecond Pulsars, Magnetars and More*, Vol. 983 of *AIP Conf. Ser.*, edited by C. Bassa, Z. Wang, A. Cumming, V.M. Kaspi (2008), p. 320, 0711.1554
73. E.V. Gotthelf, J.P. Halpern, J. Alford, *ApJ* **765**, 58 (2013), 1301.2717
74. A. Abramowski, F. Acero, F. Aharonian, A.G. Akhperjanian, G. Anton, A. Balzer, A. Barnacka, U. Barres de Almeida, A.R. Bazer-Bachi, Y. Becherini et al., *ApJ* **735**, 12 (2011), 1104.2548
75. W.W. Tian, D.A. Leahy, M. Haverkorn, B. Jiang, *ApJ* **679**, L85 (2008), 0801.3254
76. D.D. Ofengeim, A.D. Kaminker, D. Klochikov, V. Suleimanov, D.G. Yakovlev, *MNRAS* **454**, 2668 (2015), 1510.00573
77. M. Gilfanov, M. Revnivtsev, S. Molkov, *A&A* **410**, 217 (2003), [arXiv:astro-ph/0207575](#)
78. M.G. Revnivtsev, M.R. Gilfanov, *A&A* **453**, 253 (2006), [arXiv:astro-ph/0506019](#)
79. N.A. Inogamov, R.A. Sunyaev, *Astronomy Letters* **25**, 269 (1999)
80. R.A. Sunyaev, L.G. Titarchuk, *A&A* **86**, 121 (1980)
81. F. Meyer, E. Meyer-Hofmeister, *A&A* **288**, 175 (1994)
82. J.J.E. Kajava, J. Nättilä, O.M. Latvala, M. Pursiainen, J. Poutanen, V.F. Suleimanov, M.G. Revnivtsev, E. Kuulkers, D.K. Galloway, *MNRAS* **445**, 4218 (2014), 1406.0322
83. I.I. Lapidus, R.A. Sunyaev, *MNRAS* **217**, 291 (1985)
84. T. Güver, P. Wroblewski, L. Camarota, F. Özel, *ApJ* **719**, 1807 (2010), 1002.3825
85. F. Özel, A. Gould, T. Güver, *ApJ* **748**, 5 (2012), 1104.5027
86. T. Güver, F. Özel, *ApJ* **765**, L1 (2013), 1301.0831
87. F. Özel, D. Psaltis, *ArXiv e-prints* (2015), 1505.05156
88. A.W. Steiner, J.M. Lattimer, E.F. Brown, *ApJ* **765**, L5 (2013), 1205.6871
89. M. AlGendy, S.M. Morsink, *ApJ* **791**, 78 (2014), 1404.0609
90. M. Bauböck, F. Özel, D. Psaltis, S.M. Morsink, *ApJ* **799**, 22 (2015)
91. V. Hambaryan, V. Suleimanov, A.D. Schwöpe, R. Neuhäuser, K. Werner, A.Y. Potekhin, *A&A* **534**, A74 (2011)